Geophysical Journal International

Geophys. J. Int. (2022) **228,** 2174–2197
Advance Access publication 2021 October 25
GJI Geodynamics and Tectonics

https://doi.org/10.1093/gji/ggab436

GPS-derived interseismic fault locking along the Jalisco–Colima segment of the Mexico subduction zone

B. Cosenza-Muralles [1,2] C. DeMets [1] B. Márquez-Azúa,[3] O. Sánchez,[4] J. Stock,[5] E. Cabral-Cano[4] and R. McCaffrey[6]

[1] *Department of Geoscience, University of Wisconsin-Madison, Madison, WI* 53706, *USA. E-mail: cosenzamural@wisc.edu*
[2] *Instituto de Investigación en Ciencias Físicas y Matemáticas, Escuela de Ciencias Físicas y Matemáticas, Universidad de San Carlos de Guatemala,* 01012 *Ciudad de Guatemala, Guatemala*
[3] *Departamento de Estudios Socio Urbanos, Universidad de Guadalajara,* 44100 *Guadalajara, Jalisco, México*
[4] *Instituto de Geofísica, Universidad Nacional Autónoma de México, Ciudad Universitaria, México CDMX* 04510, *México*
[5] *Caltech Seismological Laboratory, California Institute of Technology, Pasadena, CA* 91125, *USA*
[6] *Department of Geology, Portland State University, Portland, OR* 97201, *USA*

Accepted 2021 October 15. Received 2021 October 8; in original form 2021 January 29

SUMMARY

Northeastward subduction of the oceanic Rivera and Cocos plates in western Mexico poses a poorly understood seismic hazard to the overlying areas of the North America plate. We estimate the magnitude and distribution of interseismic locking along the northern ∼500 km of the Mexico subduction zone, with a series of elastic half-space inversions that optimize the fits to the velocities of 57 GPS stations in western Mexico. All velocities were corrected for the co-seismic, afterslip and viscoelastic rebound effects of the 1995 Colima–Jalisco and 2003 Tecomán earthquakes. We explore the robustness of interseismic locking estimates to a variety of mantle Maxwell times that are required for the viscoelastic corrections, to the maximum permitted depth for locking of the subduction interface and to the location assigned to the Rivera–Cocos–North America plate triple junction offshore from western Mexico. The best-fitting locking solutions are associated with a maximum locking depth of 40 km, a triple junction location ∼50 km northwest of the Manzanillo Trough and a mantle Maxwell time of 15 yr (viscosity of 2×10^{19} Pa s). Checkerboard tests show that the locking distribution is best resolved at intermediate depths (10–40 km). All of our inversions define a gradual transition from strong locking (i.e. 70–100 per cent) of most (70 per cent) of the Rivera–North America subduction interface to strong but less uniform locking below the Manzanillo Trough, where oceanic lithosphere transitional between the Cocos and Rivera plate subducts, to weak to moderate locking (averaging 55 per cent) of the Michoacán segment of the Cocos–North America interface. Strong locking of the ∼125-km-long trench segment offshore from Puerto Vallarta and other developed coastal areas, where our modelling indicates an average annual elastic slip-rate deficit of ∼20 mm yr^{-1}, implies that ∼1.8 m of unrelieved plate slip has accrued since the segment last ruptured in 1932, sufficient for an $M \sim 8.0$ earthquake.

Key words: Plate motions; Earthquake hazards; Seismic cycle; Space geodetic surveys; Subduction zone processes.

1 INTRODUCTION

Geodetic studies of the Jalisco–Colima subduction zone (JCSZ) began in the mid-1990s with aims of monitoring interseismic strain accumulation and crustal deformation associated with the subduction of the Rivera (RI) and Cocos (CO) plates beneath the North America (NA) plate (Fig. 1). At the time, the RI plate subduction zone had been relatively aseismic since the destructive June 3 1932 ($M_w = 8.2$) and June 18 1932 ($M_w = 7.8$) earthquakes, most likely indicating that the subduction interface was relocked and accumulating strain for a future large earthquake. DeMets *et al.* (1995) suggested that the seismic energy that was released by the 1932 earthquakes could reaccumulate in ∼80 yr given an average estimated plate kinematic convergence rate of 20–30 mm yr^{-1} (DeMets & Stein 1990). Since then, two large earthquakes, the $M_w = 8.0$ 1995 October 9 Colima–Jalisco and $M_w = 7.4$ 2003 January 22 Tecomán earthquakes have ruptured roughly half of the subduction interface that ruptured in 1932. The northwestern ∼120 km

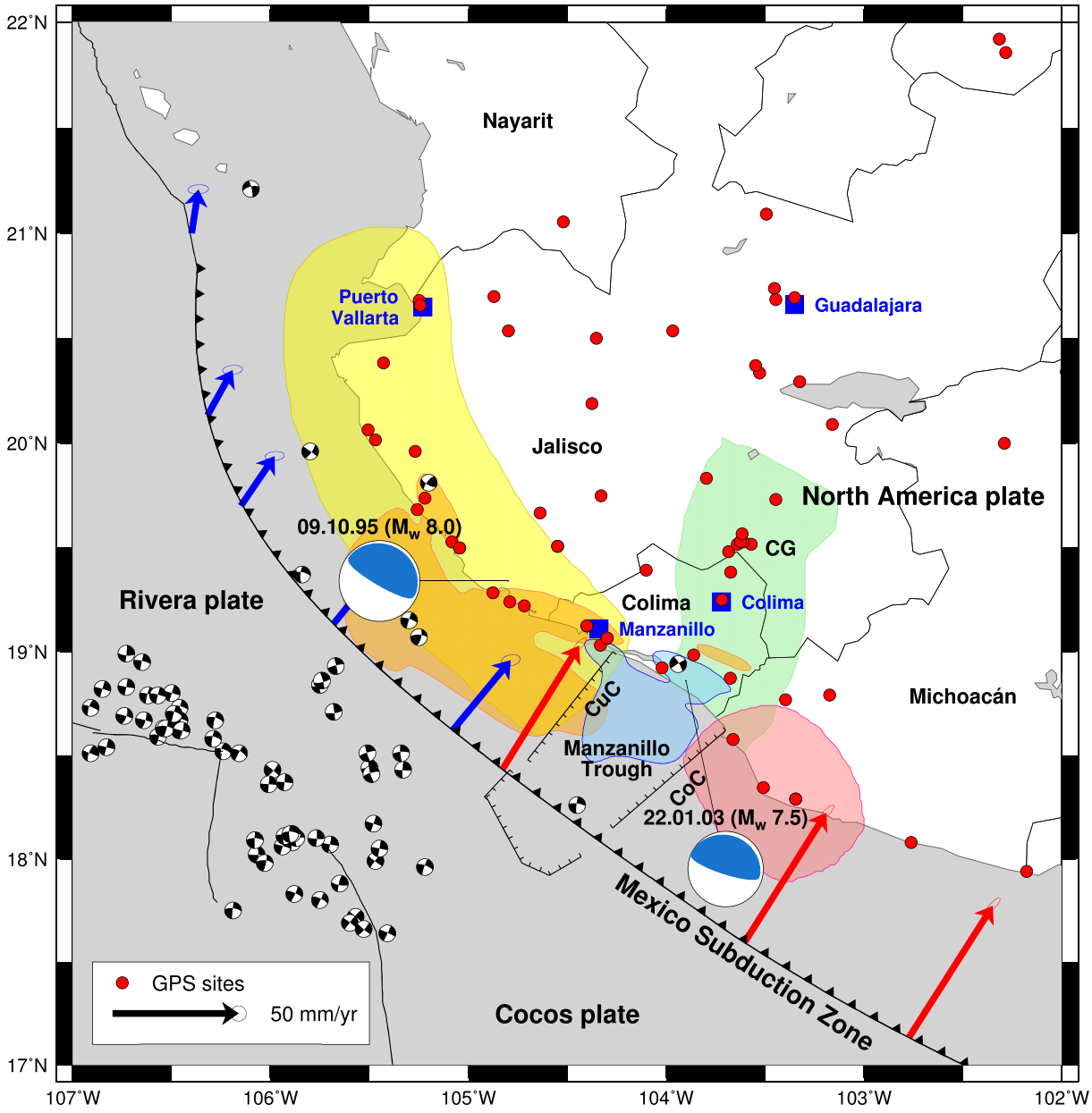

Figure 1. Tectonic setting with focal mechanisms for the 1995 Colima–Jalisco and the 2003 Tecomán earthquakes (blue and white) and for $M_w \geq 4.0$ strike-slip earthquakes with depths ≤60 km from 1976 to 2020 (black and white) from the Global Centroid Moment Tensor (gCMT) catalogue. Arrows indicate velocities of CO (red) and RI (blue) plates relative to NA plate, as predicted by the MORVEL global plate motion model (DeMets *et al.* 2010). Red dots show the location of the GPS sites. Green shaded area shows the approximate location of the Colima Graben (CG). CoC: Coahuayana canyon. CuC: Cuyutlán canyon. Shaded areas show the rupture areas of the two 1932 (yellow, Singh *et al.* 1985), the 1973 (red, Reyes *et al.* 1979), the 1995 and 2003 (orange and blue, Cosenza-Muralles *et al.* 2021) earthquakes.

of the 1932 rupture zone, offshore from Puerto Vallarta and other major tourist resorts along Jalisco's Gold Coast, has however remained seismically quiescent and presumably remains a seismic hazard.

Efforts to quantify steady-state interseismic strain accumulation and interseismic coupling across the RI–NA subduction interface and northwesternmost few hundred km of the CO–NA subduction interface, which are essential for understanding the regional seismic hazard, have been impeded by transient deformation associated with the 1995 and 2003 earthquakes. Prior to our two-part study of this area, only two studies have estimated interseismic locking in the region. From the velocity of a single continuous GPS site COLI that operated for ∼2.5 yr before the 1995 Colima–Jalisco earthquake, Marquez-Azua *et al.* (2002) estimated that the shallow regions of the RI/NA subduction interface (depths < 25 km) were fully locked prior to the earthquake. Selvans *et al.* (2011) approximated the steady interseismic velocity field from GPS data gathered in western Mexico between 1998 and 2001 based on the assumption that transient deformation from the 1995 earthquake had decayed to negligible levels by early 1998. Because most of their estimated site velocities pointed towards the subduction zone, opposite to the inland-directed motion expected for a region with

interseismic elastic shortening, Selvans *et al.* (2011) concluded that their site velocities included a component of viscoelastic rebound from the 1995 earthquake.

This study is the second stage of a two-part seismotectonic study of northwestern Mexico. In the first part, we inverted the 1993–2020 daily position time-series of 62 GPS sites in western Mexico to estimate time-dependent co-seismic slip and post-seismic afterslip solutions for the 1995 Colima–Jalisco and 2003 Tecomán earthquakes and interseismic GPS site velocities fully corrected for the viscoelastic deformation triggered by both earthquakes (Cosenza-Muralles *et al.* 2021). Hereafter, we refer to the first-stage study as CM21-I. In this second part, we describe and invert the long-term interseismic station velocities estimated by CM21-I in order to estimate the magnitude of interseismic locking along the RI/NA and CO/NA subduction interfaces (Fig. 1), determine whether the interseismic locking differs significantly between the two subduction interfaces, and identify where interseismic locking occurs in relation to post-seismic afterslip and non-volcanic tremor. An important aspect of this study is to evaluate the sensitivity of our estimated locking solutions to the following: (1) The mantle viscosities that were used by CM21-I to correct the GPS time-series. (2) The location assumed for the poorly understood offshore boundary between the subducting RI and CO plates. (3) The maximum depth for interseismic locking of the subduction interface. (4) The estimated convergence rate between the RI and NA plates.

2 TECTONIC SETTING

JCSZ, at the northern end of the Mexico subduction zone (MSZ) and offshore from western Mexico, accommodates northeastward subduction of the RI and CO plates beneath the western edge of the NA plate (Fig. 1). The RI plate subducts beneath NA along a 270-km trench segment northwest of the RI–CO–NA trench–trench–fault triple junction, transitioning from 36.0 ± 2.2 mm yr^{-1} of nearly perpendicular subduction at 18.6°N, 105.1°W to slower, more oblique subduction to the northwest, reaching 17.6 ± 1.3 mm yr^{-1} at 21.0°N, 106.4°W (DeMets *et al.* 2010). Farther southeast along the trench, the CO plate subducts northeastwards at rates as slow as 57.6 ± 2.6 mm yr^{-1} offshore from the southern Colima Graben at 18.4°N, 104.9°W (Fig. 1).

A key unknown in the regional plate motions is the location of the boundary between the subducting RI and CO plates. Based on the existence of a ∼100-km-wide seismic zone between the trench and East Pacific Rise near 105–105.5°W and the numerous strike-slip earthquakes within that zone (Fig. 1), DeMets & Wilson (1997) propose that the movement between the two plates outboards from the trench is accommodated across a diffuse boundary that intersects the trench between ∼19°N and 18°N. The location and nature of the subducted portion of the RI–CO plate boundary below the continent are poorly understood. Offshore from the southern Colima Graben (Fig. 1), reflection seismic profiles image numerous normal faults that offset the shelf/slope sediments in this subsiding region and at least one prominent strike-slip fault (Bandy *et al.* 2005). The proximity of these upper plate faults to the zone of diffuse shear west of the trench suggests that they are an upper plate expression of the differential movement between the CO and RI plates below the continent. Some evidence favours a relatively narrow boundary below the southern Colima Graben and the adjacent offshore deforming zone (Singh *et al.* 1985; Bandy *et al.* 1995,1998; Alvarez & Yutsis 2015).

Later in the analysis, we explore the influence of different assumed RI–CO boundary locations on our results. For simplicity, we refer to the tectonically active submarine area offshore from the southern Colima Graben as the Manzanillo Trough, with the caveat that this feature, which is bounded by the Cuyutlán and Coahuayana submarine canyons (Fig. 1), encompasses multiple active and inactive structures (Bandy *et al.* 2005).

3 DATA

3.1 Raw GPS data and processing

For our two-part study, we compiled all available GPS data from western Mexico, including all the data that were used in previous geodetic studies of this region (e.g. Melbourne *et al.* 1997; Hutton *et al.* 2001; Marquez-Azua *et al.* 2002; Melbourne *et al.* 2002; Schmitt *et al.* 2007; Selvans *et al.* 2011) and all subsequent observations. Detailed information about our GPS data processing methods, GPS site locations, data time spans, and position time-series, and the inversions we used to simultaneously estimate the co-seismic offsets of the 1995 and 2003 earthquakes, their time-dependent post-seismic fault afterslips, and the long-term interseismic GPS site velocities after correcting for post-seismic viscoelastic effects of both earthquakes are given by CM21-I. The viscoelastic effects of the 1995 and 2003 earthquakes estimated by CM21-I were calculated for six different characteristic decay times for a viscoelastic mantle of Maxwell rheology (i.e. $\tau_m = 2.5$, 4, 8, 15, 25, and 40 yr, corresponding to upper mantle viscosities η of 3×10^{18}, 5×10^{18}, 1×10^{19}, 3×10^{19}, and 5×10^{19} Pa s, respectively).

The horizontal velocities used herein are specified relative to the NA plate, whose motion is given by an angular velocity that best fits the motions of ∼1000 continuous GPS stations in the plate interior (CM21-I). Larger than expected values of the misfit functions from the CM21-I inversions suggest that the data uncertainties are undervalued. For example, the formal velocity uncertainties estimated from the inversions described in CM21-I do not account for likely errors or biases that might be introduced by the CM21-I viscoelastic corrections and assumptions, including our geodetic definition of the NA plate frame of reference. CM21-I, thus, systematically increased the formal uncertainties, which were typically only fractions of a mm yr^{-1}, to more typical magnitudes of ± 3 mm yr^{-1} in the horizontal components and larger in the vertical component. In Section 5.2.5, we also consider how our results might change due to a possible bias in our geodetic definition of the NA plate. All of the velocities and uncertainties that were used for this analysis are found in the materials provided in the Supplementary Information of CM21-I.

3.2 GPS site velocities

62 GPS sites were active in our study area between 1993 and 2020, consisting of 36 continuous and 26 campaign sites. Of these, we excluded from this analysis the velocities of four sites with too few observations to be useful (LIMA, TNZA, TOMA and VALL) and one site (NOVI) with a velocity that disagreed significantly with the velocities of other more reliable nearby sites. Fig. 2 displays the 3-D velocities (black arrows) of the remaining 57 sites, all corrected for the co-seismic and afterslip effects of the 1995 and 2003 earthquakes, and the viscoelastic effects of each earthquake assuming a mantle Maxwell time τ_m of 15 yr (with an equivalent mantle viscosity of 2×10^{19} Pa s for a shear modulus μ of 40 GPa).

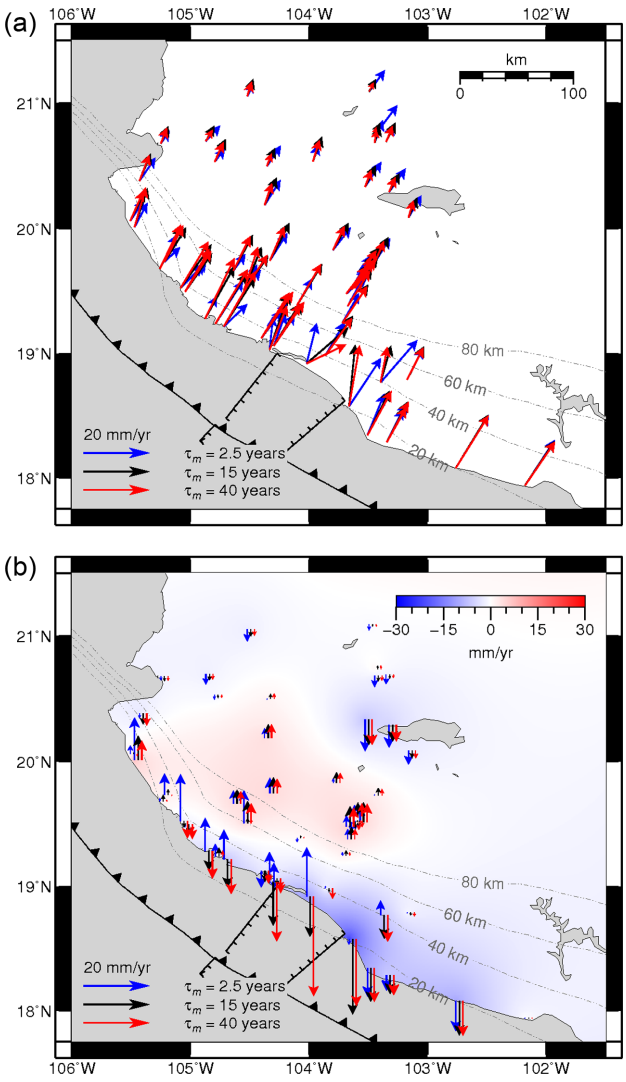

Figure 2. Best-fitting GPS site velocities from the time-dependent inversions of GPS position time-series that were corrected for the viscoelastic effects of the 1995 Colima–Jalisco and 2003 Tecomán earthquakes using mantle Maxwell times τ_m of 2.5 yr (blue), 15 yr (black) and 40 yr (red). (a) Horizontal velocities relative to a fixed NA plate frame of reference. (b) Vertical velocities. Colour shows the interpolated surface vertical velocities over the region for the case of $\tau_m = 15$ yr, as in Supporting Information Fig. S4. Uncertainties were omitted for clarity.

The horizontal velocities (Fig. 2a) are dominated by northeastward motion toward the plate interior at rates that diminish rapidly inland from the trench (Figs 3a and b). The vertical rates transition from subsidence in coastal areas to slow uplift at locations farther inland (Figs 2b and 3c & d). The observed margin normal shortening is consistent with elastic strain that arises from partial to full coupling of the Mexico subduction interface.

Much of the ensuing analysis is based on inversions of the CM21-I interseismic velocities based on an assumed τ_m of 15 yr (black arrows in Fig. 2; black circles in Fig. 3, and table S12 of CM21-I), which are associated with the best overall wrms model fits in our two-part study. We also present results from inversions of the CM21-I interseismic velocities that are associated with mantle Maxwell times of 2.5–40 yr (section 3.1 and table S12 of CM21-I). The CM21-I inversions for these mantle Maxwell times variously fit the GPS position time-series as well as or up to 10 per cent worse than for $\tau_m = 15$ yr. Supporting Information Figs S1–S7 display the CM21-I velocity fields for assumed mantle Maxwell times of 2.5, 4, 8, 25 and 40 yr, and a velocity field without any viscoelastic correction. These velocity fields are dominated by northeast-directed stations motions, like the $\tau_m = 15$ yr velocity field, but have different velocity magnitudes and gradients. Figs 2 and 3 compare the end member velocity fields for corrections that use $\tau_m = 2.5$ and 40 yr. For $\tau_m = 40$ yr, the trench-normal rates of sites in the coastal areas of Jalisco (Figs 3a and b) average 14–19 mm yr^{-1} and diminish to only 3 mm yr^{-1} ∼250 km inland. Along the same transect, the coastal site velocities for $\tau_m = 2.5$ yr decrease from 7–10 to 5–7 mm yr^{-1} ∼250 km inland (Fig. 3, Supporting Information Figs S1 and S6). The velocity magnitudes and gradients, which are critical for estimating the magnitude and depth distribution of interseismic locking, thus differ significantly with mantle viscosity.

Similar large differences occur for the $\tau_m = 2.5$ yr versus $\tau_m = 40$ yr vertical rates (Figs 3c and d, Supporting Information Figs S1 and S6). Whereas the $\tau_m = 2.5$ yr vertical rates for a trench-normal transect of the Jalisco region transition from coastal subsidence to inland uplift, the $\tau_m = 40$ yr vertical rates transition from rapid coastal uplift to slow or no uplift farther inland. Estimates of the 3-D velocities and the interseismic locking models we derive from them are thus sensitive to the mantle Maxwell time (or viscosity) that was used to calibrate those velocities for the viscoelastic effects of the 1995 and 2003 earthquakes. The analysis below describes how our primary results vary for the full range of Maxwell times that were used in CM21-I.

For completeness, we also calculated a velocity field based on the assumption that all the transient effects of the 1995 and 2003 earthquakes had diminished sufficiently by 2010 so that the station measurements after 2010 once again closely approximated the long-term interseismic station velocities. We estimated best-fitting 3-D slopes for each station with measurements after 2010 from the original daily station positions corrected only for the steady movement of the NA plate. Supporting Information Figs S8(a) and (c) compare the horizontal and vertical velocities to the 1995–2020 velocities that are fully corrected for the transient effects of both earthquakes using a mantle Maxwell time of 15 yr. The differences between the two velocity fields (Supporting Information Figs S8b and d) argue strongly for a significant viscoelastic contribution to the station motions after 2010. Relative to the corrected station velocities (blue arrows in Supporting Information Fig. S8a), all the inland stations move more slowly toward the interior (red arrows in the figure). The differential station velocities point directly toward the 1995/2003 rupture zones and include an outward-radiating component at coastal locations that are nodal to the rupture zones (Supporting Information Fig. S8b). This pattern strongly resembles the net viscoelastic response computed from the 1995 and 2003 coseismic slip solutions (fig. S12 in CM21-I). The differential vertical site rates (Supporting Information Fig. S8d), which are dominantly downward, also agree with the computed viscoelastic response from CM21-I. Absent any corrections for transient post-seismic deformation, the velocities recorded after 2010 at stations in our study area are thus unsuitable for estimating subduction zone locking solutions. A good example of this is the post-2010 motion at site COLI (see fig. 3 in CM21-I for COLI's GPS position time-series), which has recovered it's linear trend but does not yet match the pre-1995 earthquake motion.

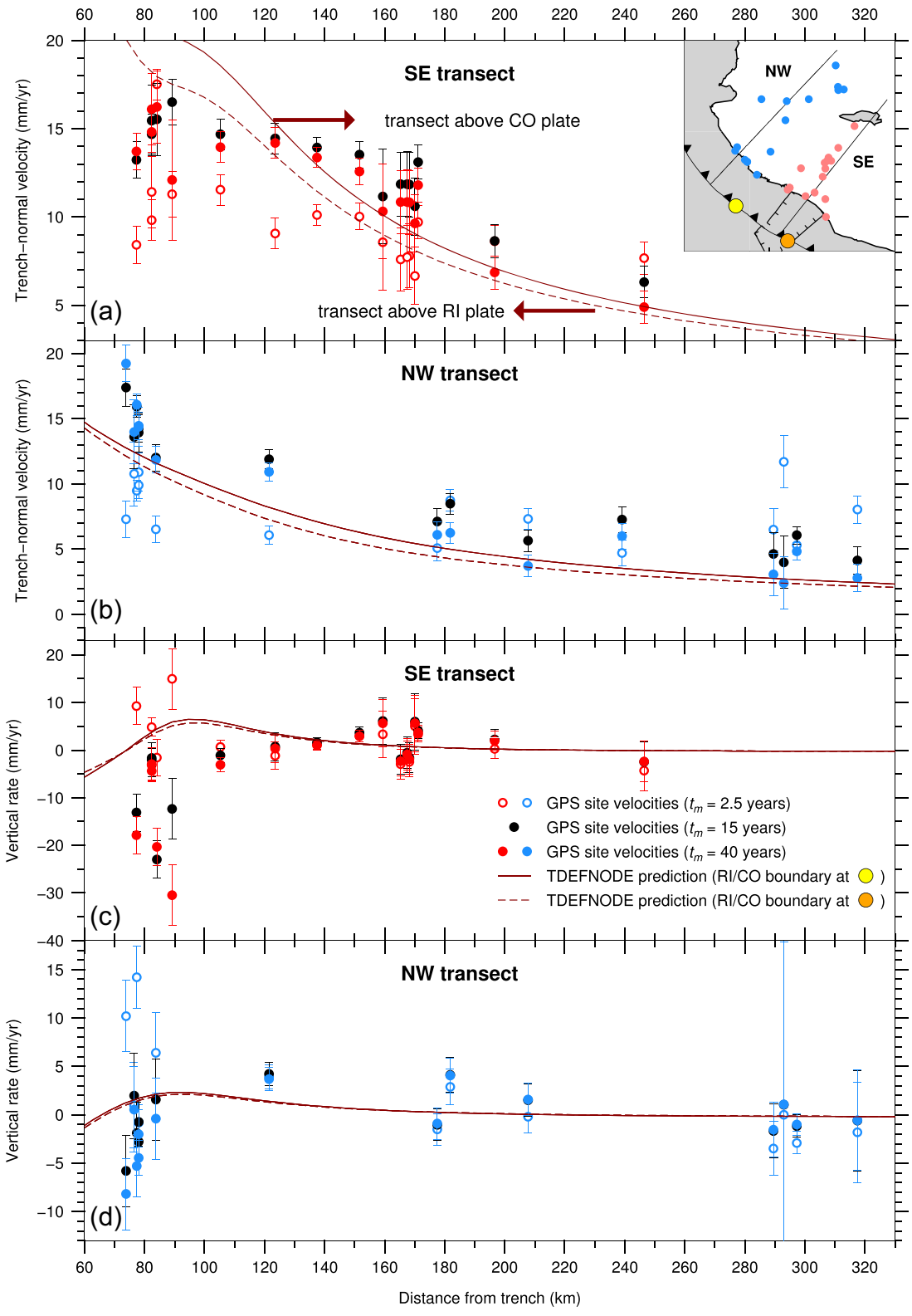

Figure 3. Trench-normal (a and b) and vertical (c and d) velocity components with 1σ uncertainties, corrected for viscoelastic effects from a mantle with $\tau_m = 2.5$ yr (open circles), 15 yr (black circles) and 40 yr (filled circles), along the northwestern (N45°E, blue) and southeastern (N40°E, red) transects in inset map. Dashed and continuous lines show TDEFNODE predictions for an interface fully locked between depths of 0 and 25 km, using RI/CO boundary locations 1 (orange circle) and 3 (yellow circle), respectively.

4 METHODS

4.1 TDEFNODE inversions

In general, interseismic GPS velocity fields are well approximated by models that incorporate rotating blocks that deform internally via interseismic elastic strain due to interactions with other blocks across the bounding faults (McCaffrey 2002). The motion of a block i rotating in the reference frame R is described by its angular velocity vector ${}_R\boldsymbol{\omega}_i = (\lambda_p, \phi_p, \omega)$, where λ_p,ϕ_p and ω specify the angular velocity's latitude, longitude and rotation rate, respectively. The horizontal velocity of each point $\mathbf{X}$ on block i relative to reference frame R is given by ${}_R\mathbf{V}_i = {}_R\boldsymbol{\omega}_i \times \mathbf{X}$, where $\mathbf{X}$ is the vector that points from the geocentre to said point. The difference in the constant velocities of blocks i and j, ${}_j\mathbf{V}_i = {}_R\mathbf{V}_i - {}_R\mathbf{V}_j$, calculated at point $\mathbf{X}$ on the fault that separates the two blocks gives the long-term slip rate at that point. Friction along the boundary between two blocks gives rise to an accruing elastic slip deficit with respect to the expected long-term block motion. The fractional part of relative plate motion that is not accommodated by steady, aseismic slip is referred to as 'locking' (McCaffrey 2002). When parts of the fault are locked, the motions everywhere within the bounding blocks due to their rotations in reference frame R are modified by elastic strain whose magnitude and direction depend on the orientation and configuration of the locked boundary faults and the rate and sense of slip across those faults.

We use TDEFNODE to estimate interseismic locking of the Jalisco–Colima subduction interface from the GPS site velocities described above. When applied in its static mode, TDEFNODE simultaneously estimates block rotations, fault locking and block strain-rate tensors (for blocks with long-term internal deformation; McCaffrey 2002). Elastic deformation is determined using backslip methods (Savage 1983) and half-space dislocation equations (Okada 1985) that quantify the direction and rate of elastic deformation given the orientations, locations, and slip sense/rate of locked faults. Faults (and hence fault locking) are parametrized by nodes that follow fault depth contours. At each fault node, a long-term fault slip-rate vector $\mathbf{V}$ is determined from the angular velocity that specifies the relative motion of the two fault-bounding blocks; backslip is applied to the fault as $\varphi\mathbf{V}$, where φ is the fault locking.

For blocks without long-term internal deformation, as we assume for this analysis, the velocities V_i at locations $\mathbf{X}$ within our study area are given by (McCaffrey 2002)

$$V_i(\mathbf{X}) = \sum_{b=1}^{B} H(\mathbf{X} \in \Delta_b)[{}_R\boldsymbol{\omega}_b \times \mathbf{X}] \cdot \hat{\mathbf{i}} - \sum_{k=1}^{\mathrm{NF}} \sum_{n=1}^{N_k} \sum_{j=1}^{2} \varphi_{nk} G_{ij}(\mathbf{X}, \mathbf{X}_{nk})[{}_h\boldsymbol{\omega}_f \times \mathbf{X}_{nk}] \cdot \hat{\mathbf{j}} \quad (1)$$

where i is the index for velocity component (x, y, or z); B is the number of blocks; Δ is the subset of the model domain within block b; $H = 1$ if the point $\mathbf{X}$ is contained within block b, $H = 0$ otherwise; $\hat{\mathbf{i}}$ is the unit vector in the ith direction; ${}_R\boldsymbol{\omega}_b$ is the angular velocity vector of block b relative to the reference frame; ${}_h\boldsymbol{\omega}_f = {}_h\boldsymbol{\omega}_R - {}_f\boldsymbol{\omega}_R$ is the angular velocity vector of the footwall block f of fault relative to the hanging wall block h; NF is the number of faults; N_k is the number of nodes defining fault k; $\mathbf{X}_{nk}$ is the position of node n on fault k; φ_{nk} is the locking fraction at node n on fault k, as defined above; $\hat{\mathbf{j}}$ is the unit vector in jth direction on fault surface (downdip or along-strike); and $G_{ij}(\mathbf{X}, \mathbf{X}_{nk})$ is the elastic response function that specifies the ith component of velocity at surface point $\mathbf{X}$ due to a unit slip velocity along fault surface at node $\mathbf{X}_{nk}$ in the jth direction.

The components of G_{ij} are the Green's functions that quantify the theoretical elastic response at each GPS site due to assumed unit slip at each fault node within the model domain (Okada 1985).

The Jalisco–Colima subduction interface geometry used herein is described by CM21-I. Fault node spacings are ∼9–27 km along-strike (∼18.5 km on average) and ∼5–25 km downdip (∼10.5 km on average), located at 5-km depth contours. The spatial distribution of locking was parametrized with TDEFNODE's independent nodes option, which estimates the locking at each node. In order to reduce the number of parameters and increase the degrees of freedom to avoid an underdetermined problem, we grouped the nodes in pairs in the downdip direction (in case of an odd number of depth contours, the last three nodes downdip were grouped). In the along-strike direction, we grouped the nodes at the ends of the subduction interface (the four southeasternmost nodes of the CO/NA interface and the five northwesternmost nodes of the RI/NA interface). We grouped the rest of the nodes in pairs in the along-strike direction, with the exception of those from about 50 km west of the Manzanillo Trough to the northwestern end of the Jalisco coast, which were treated as independent along-strike and were only grouped in the downdip direction. Thus, a single locking value is estimated for each group of nodes. We did not use any constraints on the variation of locking with depth.

Misfit F is defined in TDEFNODE as the sum of the reduced chi-squared statistic (χ^2_ν), which is a data misfit penalty function, and the penalties associated with smoothing (McCaffrey 2002, 2005):

$$F = \chi^2_\nu + \text{penalties} = \frac{1}{\nu}\mathbf{R}^{\mathrm{T}}\mathbf{C}^{-1}\mathbf{R} + A_1\left(\frac{\mathrm{d}^2\varphi}{\mathrm{d}x^2}\right)^2 + A_2\left(\frac{\mathrm{d}^2\varphi}{\mathrm{d}w^2}\right)^2 \quad (2)$$

where ν represents the degrees of freedom (number of observations N minus number of parameters); $\mathbf{R}$ is the matrix of velocity residuals (R_e, R_n, R_v), T indicates the transpose of the matrix, $\mathbf{C}$ is the east–north–vertical covariance matrix, x and w denote, respectively, the along-strike and downdip directions; A_1 and A_2 are the smoothing factors that scale the penalties along-strike and downdip, respectively, and φ is the locking coefficient. The misfit function F is minimized through simulated annealing and grid search iterations. As is shown in eq. (2), we applied Laplacian (i.e. second derivative) smoothing both in the along-strike and downdip directions during our static TDEFNODE inversions in order to avoid short-wavelength artefacts in our locking solutions. We explored a variety of smoothing factors to mitigate the trade-off between the misfit and the model complexity.

The motions of two of the three plates in our TDEFNODE model, the CO and RI plates, are specified *a priori* relative to the NA plate by the MORVEL CO–NA and RI–NA angular velocities (DeMets *et al.* 2010; Table 1). Later in the analysis, we evaluate how our results change if the poorly known RI–NA angular rate is increased or if we adopt an alternative NA plate geodetic frame of reference for the GPS site velocities.

4.2 Model resolution

We tested the ability of the GPS network in western Mexico to resolve locking along the JCSZ via a checkerboard test, with locking distributed in rectangular patches of alternating constant values of 0 and 0.5 (Fig. 4). We calculated synthetic 3-D velocities from two different starting models at each site of the GPS network, perturbed the synthetic velocities with random noise of 1 mm yr^{-1} (1σ) for the east and north components and 2 mm yr^{-1} for the vertical

Table 1. Angular velocity vectors of the three plates used in our inversions.

Plate	Reference frame	Angular velocity vector: Latitude (°N)	Longitude (°E)	Rate ω (° Myr^{-1})	Source
North America	ITRF14	7.45	92.04	0.183×10^{-6}	CM21-I
Rivera	NA	21.3	−108.6	4.369	MORVEL (DeMets *et al.* 2010)
Cocos	NA	31.1	−133.2	1.085	MORVEL (DeMets *et al.* 2010)

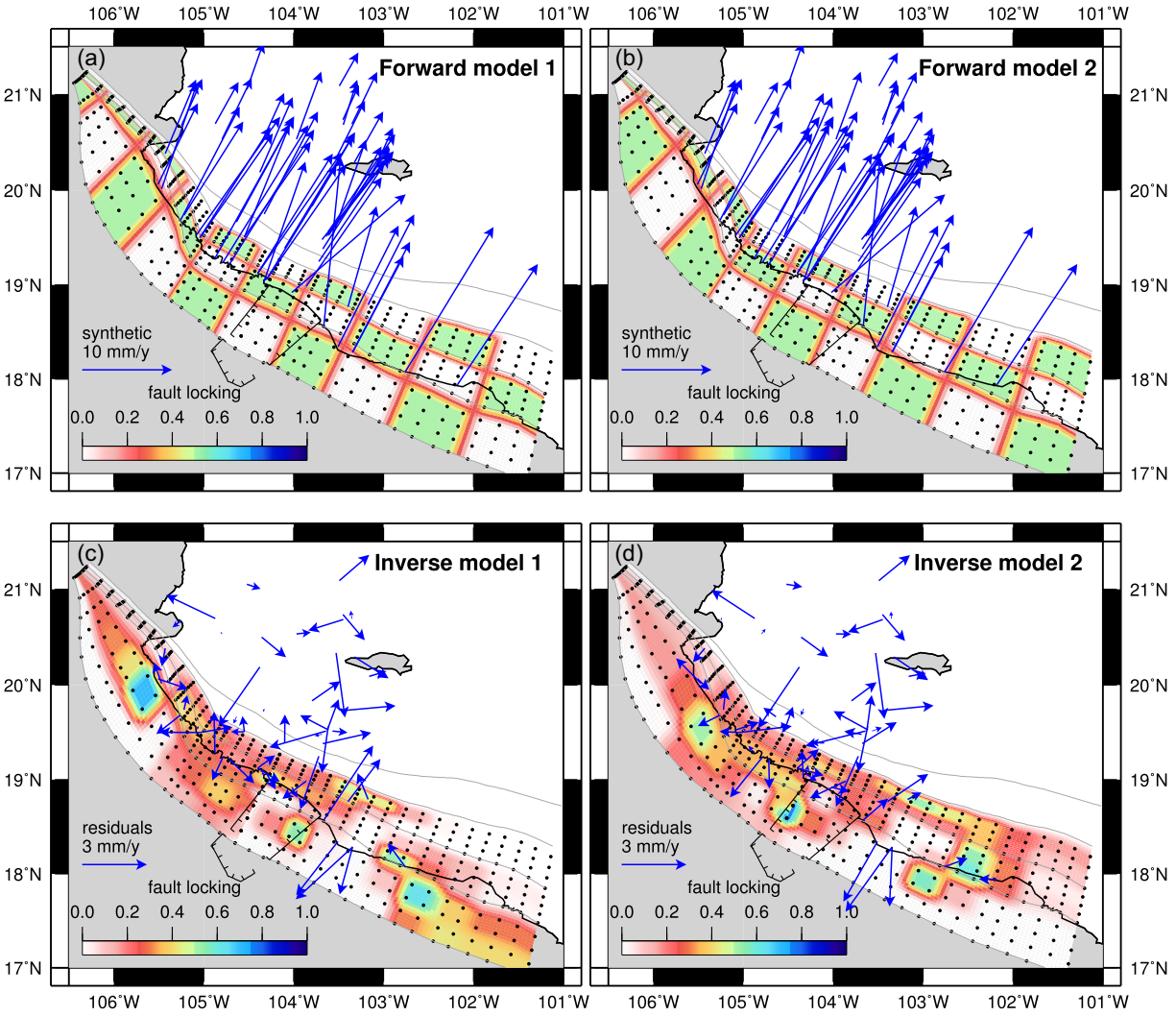

Figure 4. Checkerboard tests for the JCSZ. Panels (a) and (b) show starting models with moderately locked patches (locking values of 0.5) and their predicted (synthetic) horizontal GPS velocities. Panels (c) and (d) show locking solutions recovered from inversions of the synthetic GPS velocities with 1σ noise added ($\sigma = 1$ mm for the north and east components, and $\sigma = 2$ mm for the vertical component) and the residuals of the horizontal site velocities from the best-fitting solutions.

component, and inverted the noisy velocities while applying the same smoothing as was used for our preferred solutions. Fig. 4 shows both starting models, their associated synthetic velocities, and the models recovered from inversions of those velocities.

Comparisons of the forward and inverse locking solutions in Fig. 4 reveal the following about our ability to resolve variations in locking along the subduction interface: (1) The recovery of the forward locking solutions is poor in the southeastern third of the study area, where only two GPS stations are located. (2) Elsewhere in our study area, variations in locking that occur parallel to the subduction interface (i.e. the along-strike locking variations) are well recovered, particularly at depths of 5–20 km, where most co-seismic slip occurs. The GPS network is thus well suited for resolving differences between the average locking of the CO–NA and RI–NA subduction interfaces. (3) The starting locking values at depths above 5–10 km are recovered erratically, as expected from a network of land-based instruments.

Based on these resolution tests, our interpretations emphasize apparent along-strike locking variations. Less emphasis is given to depth-dependent locking variations; we instead interpret many of our results in terms of locking that is averaged over larger segments of the subduction interface. Several of our models require strong

locking of the RI–NA interface at nearly all depths in order to match the observed GPS velocities (Section 5.2). For this subset of models, we consider locking at shallow interface depths (depths above 10 km) to be a robust feature of the model.

4.3 Model parameter exploration

As part of our analysis, we evaluated the effect of the assumed maximum interface locking depth on our results. Pardo & Suárez (1995) estimate a ∼40 km downdip limit for seismogenic coupling of the RI/NA subduction interface and ∼25 km downdip limit for the CO/NA subduction interface below Michoacán, both from earthquake hypocentre locations and focal mechanisms. From an augmented database relative to that used by Pardo & Suárez (1995), Martínez-López & Mendoza (2016) estimate a maximum coupling depth of ∼40 km for both segments, comparable to a 35 km downdip limit estimated from seismic tomographic imaging of the subduction interface below Jalisco (Watkins *et al.* 2018). Based on these estimates, we tested the effect of varying the maximum locking depth of the subduction interface from 25 to 45 km.

We also evaluated how the fits and results are affected by the assumed location of the offshore oceanic boundary between the RI and CO plates, which determines which of the two plates is located offshore from and beneath different parts of our study region. As is shown in Fig. 5(a), we tested three possible locations for the RI–CO–NA triple junction: one each near the eastern and western limits of the Manzanillo Trough and one ∼50 km farther northwest (indicated respectively by locations 1, 2 and 3 in the map inset in Fig. 5a). All three locations fall within the region of diffuse seismicity between the trench and East Pacific Rise (Fig. 5a), which DeMets & Wilson (1997) interpret as evidence for a diffuse oceanic RI/CO boundary in this region. We did not test a model that approximates the boundary as diffuse, as seems most likely because doing so would introduce assumptions and adjustable parameters that would be difficult to resolve from the onland GPS data.

5 RESULTS

Seven GPS velocity fields were produced during the first stage of our analysis (CM21-I), one for each of the six mantle Maxwell times we explored and a seventh assuming that no viscoelastic deformation occurred (Supporting Information Figs S1–S7). In order to identify a best interseismic locking solution and its uncertainties, we did 84 trial inversions of the seven velocity fields for all three RI–CO boundary locations identified in Fig. 5(a) and four *a priori* maximum locking depths from 25–45 km. The ensuing description of our results is focused on identifying the solutions that yield the best fits and determining the robust features of the interseismic locking solutions and the sensitivities of the estimated locking solutions to the input data and assumptions. The analysis concludes with an examination of the sensitivities of the fits and results to the possible biases in the RI–NA and NA–ITRF14 angular velocities that are the basis for the plate-based frames of reference used for our analysis.

5.1 Model fits and determination of a best-fitting solution

Fig. 5 summarizes the misfits F (eq. 2) for all the velocity fields, maximum locking depths, and RI/CO boundary locations considered for our analysis, totalling 84 distinct inverse solutions. The worst fits occur for models that restrict interseismic locking to depths shallower than 25 km (Figs 5b–d), independent of the assumed RI/CO boundary location and mantle Maxwell time that was used for the velocity field calibration. For six of the seven velocity fields, the best fit occurred when interseismic locking was restricted to depths shallower than 40 km (Figs 5b–d). Notably, most of the inversions with a locking depth limit of 40 km had misfits that were ∼40 per cent smaller than the inversions with a 25-km locking depth limit. The data thus strongly favour a maximum subduction locking depth of 40 km independent of the assumed mantle Maxwell time and RI/CO plate boundary location.

For the models with a 40-km locking depth limit, the worst fits all occur for velocity fields with no correction for viscoelastic deformation (black symbols in Figs 5b–d) or short Maxwell times ($\tau_m = 2.5$ and 4 yr, corresponding to upper mantle viscosities of 3–5 $\times$ 10^{18} Pa s). The poor fits partially corroborate results that are reported in the first stage of our analysis (CM21-I), whereby the worst wrms fits from time-dependent inversions of the position time-series for GPS sites in our study area (respectively 5.8 and 6.1 mm) were associated with data that were corrected assuming τ_m of 2.5 yr or not corrected for any viscoelastic deformation. As is shown in Figs 5(b)–(d), the misfits for velocities associated with $\tau_m = 4$ yr are 35–100 per cent higher than for the best models. These poor fits suggest that the viscosity of the upper mantle below our study area is unlikely to be less than 1 $\times$ 10^{19} Pa s or greater than 1 $\times$ 10^{20} Pa s (i.e. $\tau_m > 80$ yr).

The fits for velocities that were derived using $\tau_m = 15$, 25 and 40 yr all differ by ∼10 per cent or less (Figs 5b–d) independent of the assumed maximum locking depth or RI/CO boundary location. The best-fitting model, with $F = 4.0$ and a wrms velocity misfit of 1.4 mm yr^{-1}, is for velocities that were corrected using $\tau_m = 40$ yr. Inversions of velocities that were corrected using $\tau_m = 15$ yr ($F =$ 4.4 and wrms = 1.4 mm yr^{-1}) and $\tau_m = 25$ yr ($F = 4.6$ and wrms = 1.5 mm yr^{-1}) give nearly equivalent fits. In the first stage of our study (CM21-I), the time-dependent inversions of the GPS position time-series that were corrected using Maxwell times of $\tau_m = 15$, 25, and 40 yr gave respective wrms misfits of 5.4, 5.7 and 5.6 mm. The only mantle Maxwell time in both stages of our analysis with wrms misfits that gave rise to models that were either the best fit or insignificantly different from the best fit was $\tau_m = 15$ yr.

We adopt as our preferred model the GPS site velocities that were calibrated using a mantle Maxwell time of 15 yr, a 40-km maximum permitted locking depth, and an RI–CO plate boundary that intersects the trench ∼50 km northwest of the Manzanillo Trough, based on a comparison of the fits for the static elastic half-space models we explored above and the time-dependent fits described by CM21-I. Fig. 6 shows map views of the observed and predicted horizontal and vertical velocities for the preferred model, their misfits, and their subduction interface locking (φ) and slip-rate deficit ($-\varphi V$) solutions. Fig. 7 shows trench-normal transects of same model predictions and observations for subsets of the GPS sites that lie above the subducted RI and CO plates. In the following sections we describe in more detail the preferred model and evaluate its robustness with respect to plausible variations in the assumed model parameters.

5.2 Comparison of the best-fitting and alternative solutions: model robustness

The most robust outcome of our analysis is the evidence for strong locking of the RI/NA subduction interface versus weak-to-moderate locking of the CO/NA interface (Fig. 6a). For ease of reference

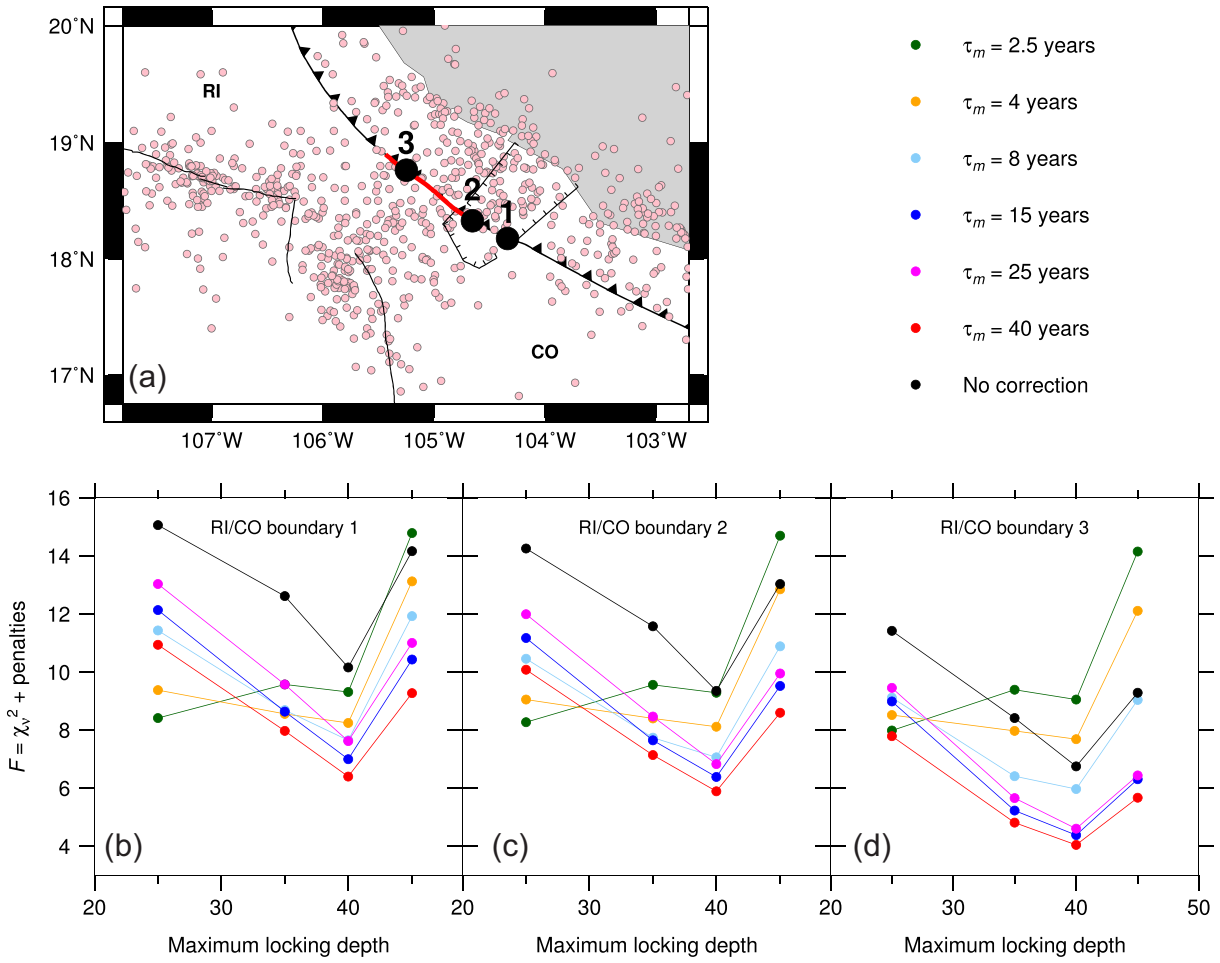

Figure 5. Misfit F versus maximum interface locking depth for models using locations 1 (b), 2 (c) and 3 (d) for the RI/CO plate boundary as shown by the black circles in (a). Red segment in (a) is the intersection of the trench with the zone of distributed shear proposed by DeMets & Wilson (1997) as a diffuse RI/CO plate boundary. Pink circles show the 1963–2017 seismicity (USGS). The circle colours in (b)–(d) identify the model misfits for GPS site velocities that were corrected for viscoelastic effects using the mantle Maxwell times τ_m defined in the legend.

below, we define a Jalisco trench segment, which corresponds to the RI–NA interface along the Jalisco coast and offshore areas, a Michoacán segment, where the CO plate subducts below NA along the state of Michoacán and offshore areas, and a Colima segment, where oceanic lithosphere with velocities likely to be transitional between the RI and CO plate motions subducts offshore from the Mexico state of Colima (Fig. 1).

Whereas ∼70 per cent of the Jalisco and Colima segments have locking values of 70–100 per cent, more than 40 per cent of the Michoacán segment subduction interface has locking values smaller than 50 per cent (Fig. 6a). This first-order difference is a direct outcome of the observation that the coastal GPS sites along the Jalisco segment move inland at rates that are the same as or 2–3 mm yr^{-1} faster than the coastal stations above the CO plate (black arrows and circles respectively in Figs 2a and 3a & b) even though the CO plate subducts at rates that are nearly 50 per cent faster than the RI plate (Fig. 1). The forward modelling predictions shown in Figs 3(a) and (b) reinforce these results. Specifically, forward models that impose full locking of the entire Jalisco segment interface everywhere between the trench and a depth of 25 km predict slower elastic shortening rates at coastal locations than are observed along the NW transect above the RI plate (Fig. 3b). Along the southeastern transect, models with full assumed interface locking predict faster-than-observed elastic shortening independent of where the RI–CO plate boundary is assumed to intersect the trench (Fig. 3a). The observations thus require strong locking to depths below 25 km along the Jalisco segment but only partial locking at depths shallower than 25 km in areas above the CO plate, consistent with our preferred model locking solution (Fig. 6a).

Our preferred model indicates that locking along the Jalisco segment averages ∼75 per cent and is distributed uniformly along-strike, whereas the locking varies more for the other two segments (Fig. 6a). Offshore from Jalisco, the interseismic locking is ≥∼90 per cent but diminishes abruptly to less than 35 per cent below the coast and continent. In contrast, the locking offshore and near the coast of the Michoacán segment (depths between 5 and 25 km) is moderate (∼65 per cent) and transitions to weak locking (<15 per cent) below the continent, at depths of 25–40 km. The weak deep locking along the Michoacán segment changes abruptly to strong locking (≥∼80 per cent) at most locations along the Colima segment. Strong locking of much of the interface northwest of and including the Manzanillo Trough is required to match the rapid northeastward velocities of the GPS sites inland from this segment (also see Fig. 3a).

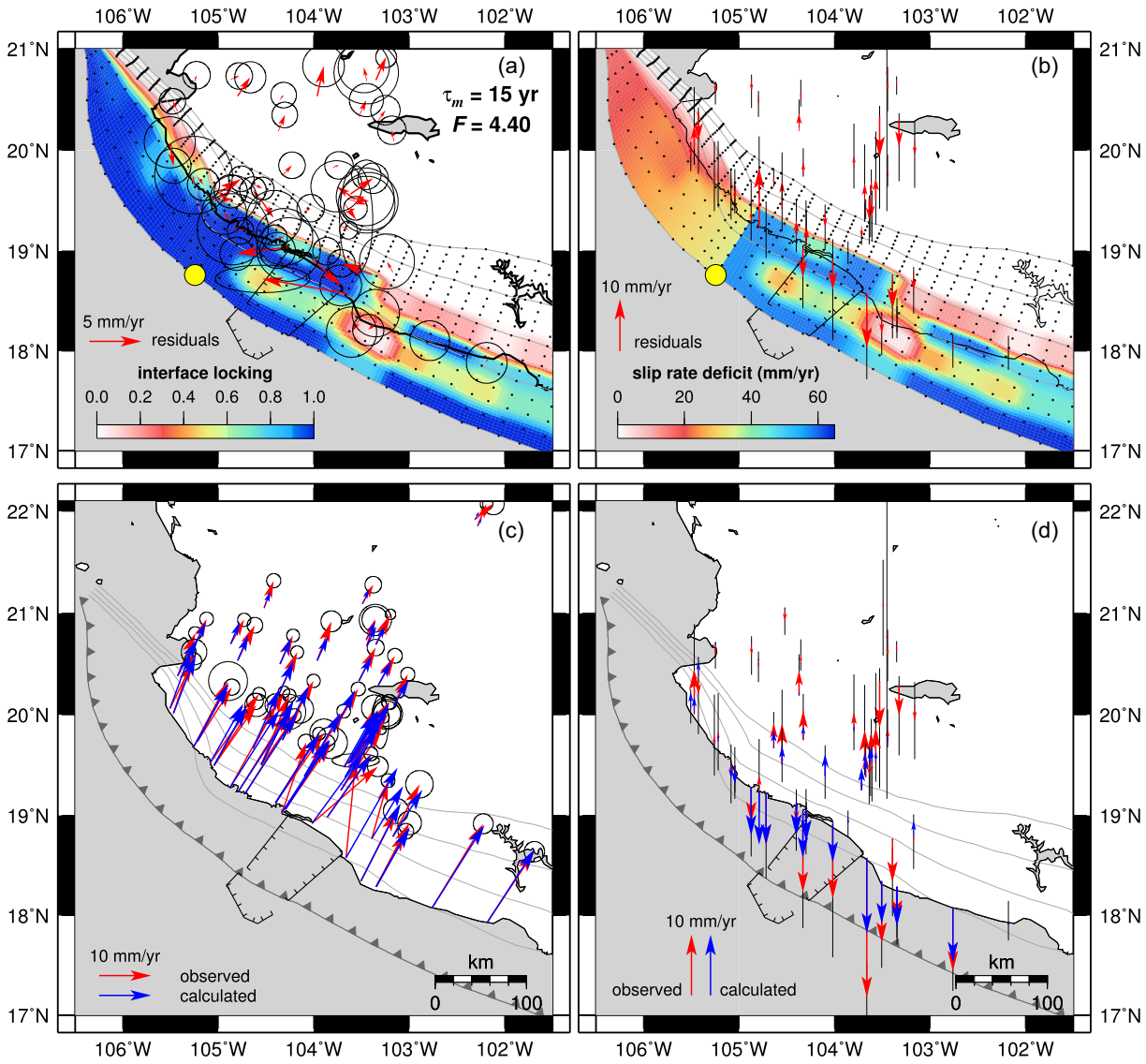

Figure 6. Interface locking (a) and slip rate deficit (b) along the Jalisco–Colima subduction zone from the best-fitting model ($\tau_m = 15$ yr, maximum locking depth of 40 km, and RI/CO plate boundary 3 from Fig. 5a). Yellow circle marks the location of the RI/CO plate boundary at the trench. Red arrows in panels (a) and (b) respectively show the horizontal and vertical velocity residuals (observed minus calculated by the model) with 1σ uncertainties (ellipses and vertical lines). Arrows in panels (c) and (d) show respectively the horizontal and vertical observed (red) and calculated (blue) velocities and their uncertainties.

Our best-fitting model also predicts that the average locking values diminish with depth (Fig. 6), from ~90 per cent at 0–10 km depths to 70 per cent at 10–25 km depths and 40 per cent below depths of 25 km. Our estimates of depth-dependent locking variations are the most reliable along the RI/NA subduction interface (Fig. 4), where the numerous GPS sites define the onshore trench-normal velocity gradient that is essential for estimating depth-dependent variations in interseismic locking on the subduction interface (Fig. 7). Strong locking all the way to the trench offshore from Jalisco appears to be necessary to fit the rapid inland velocities that are observed everywhere onshore from the subducting RI plate (e.g. Fig. 7b). Our estimates of the locking variations with depth are the least reliable along the subduction interface east of the Manzanillo Trough, where there are too few GPS sites to define the trench-normal velocity gradient (Figs 1 and 4).

The fits of our preferred model (i.e. $\tau_m = 15$ yr) to the horizontal velocity components are good, with wrms east and north velocity components misfits of 1.2 and 1.1 mm yr^{-1}, respectively (Fig. 6c). The sites with the largest misfits are situated along the coast near the limits of the 1995 and 2003 earthquake ruptures (Fig. 6c), where the estimated site velocities are the most sensitive to the accuracy of the time-dependent co-seismic, afterslip and viscoelastic corrections that were required in order to estimate the long-term station motions. We ascribe these larger misfits to likely inaccuracies in those corrections and likely oversimplifications in our models and assumptions. In general, the velocities for sites above the subducting CO plates are fit within their estimated uncertainties (Figs 7a and c). In contrast, the velocities of sites in Jalisco above the subducting RI plate are systematically faster by 1–2 mm yr^{-1} than the predicted velocities everywhere between the coast and regions far inland (Figs 6a and 7b). In the following sections, we examine possible reasons for this systematic misfit, including whether the present RI–NA convergence rate is faster than that estimated with the MORVEL angular velocity, or whether our NA–ITRF14 angular velocity is biased by glacial isostatic rebound (GIA) which impacts the GPS velocities used for our inversions.

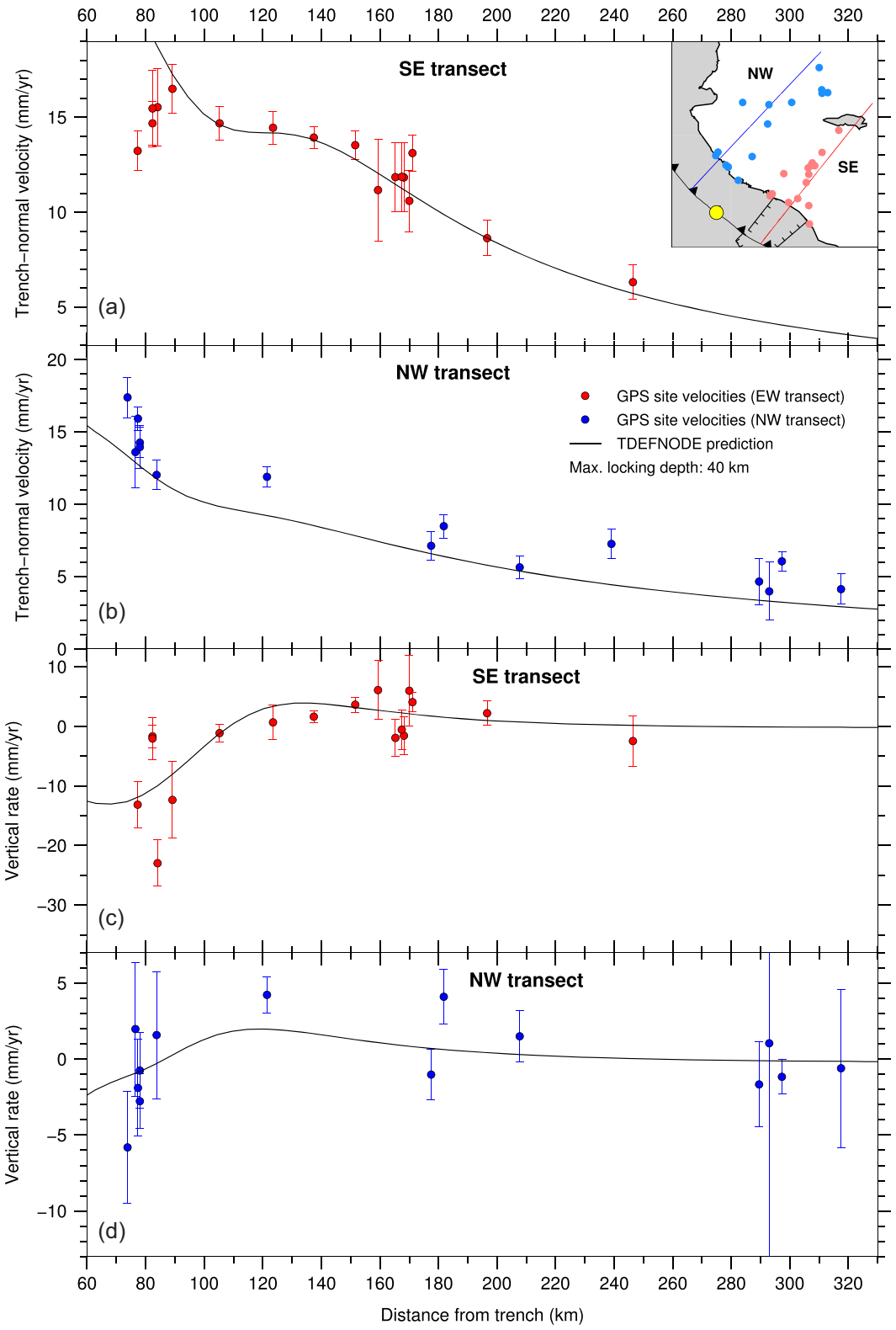

Figure 7. Fits of the preferred TDEFNODE model (black line) for the trench-normal (a and b) and vertical (b and d) velocity components with 1σ errors along the southeastern (N40°E, red) and northwestern (N45°E, blue) transects shown on inset. Yellow circle shows the location of the RI/CO boundary.

In general, the vertical rates in our study area are well fit (Figs 6d and 7c & d). The vertical rates above the CO plate (Figs 2b and 7c), nearly half of which are from continuous measurements and have uncertainties smaller than ±1–2 mm yr^{-1}, define a clear transition from subsidence at sites within 40 km of the coast to slow uplift farther inland. Given that interseismic subsidence typically occurs in areas of the continent above locked portions of the subduction interface, the pattern of vertical rates onshore from the Colima

segment usefully constrains the downdip limit of interseismic locking to ∼40 km, consistent with our preferred model.

5.2.1 Influence of viscoelastic corrections on model outcomes and fits

Fig. 8 shows the locking solutions from models with a fixed maximum interface locking depth of 40 km, an RI/CO boundary location ∼50 km northwest of the Manzanillo Trough (location 3 in Fig. 5a), and all six mantle Maxwell times. The main features of the preferred locking distribution (Figs 6a and 8d) are reproduced for all models with $\tau_m > 8$ yr (Figs 6c, e and f). A comparison of the residuals displayed in Fig. 8 and velocity transects in Figs 9(a) and (b) shows that the horizontal velocity misfits are significantly worse for shorter Maxwell times (2.5 and 4 yr) than for $\tau_m > 8$ yr. The inversions of velocities corrected for $\tau_m = 2.5$, 4 or 8 yr each misfit their data systematically (Figs 8a–c), either indicating that the average mantle viscosity exceeds 1×10^{19} Pa s or that one or more of our model assumptions are incorrect.

5.2.2 Influence of the maximum locking depth of the subduction interface

Fig. 10 illustrates how the locking solutions vary as a function of the maximum allowed locking depth for an assumed τ_m of 15 yr and RI/CO plate boundary located at its preferred site (location 3 in Fig. 5a). The primary features of our preferred model, that is nearly uniform strong locking of the Jalisco segment and patchier locking of the Michoacán segment, are robust with respect to the maximum permitted locking depth. The model with a maximum 25-km locking depth systematically underestimates the velocities of nearly all the sites in Jalisco (Figs 10a and 11a & b). By implication, the measured shortening rates are faster than can be matched via full locking of the subduction interface at the maximum plate tectonic convergence rates (Figs 11a and b). In contrast, models with maximum locking depths of 35, 40 and 45 km fit the data well, with the lowest misfit value F and hence best overall fit associated with a maximum locking depth of 40 km (Fig. 5). The along-strike change from weak to strong coupling in our preferred model is reproduced independent of our choice of maximum locking depth (Fig. 10), illustrating the robustness of this result. The TDEFNODE model predictions for an assumed 25-km locking depth differ from the rates predicted by the other models by up to 10 mm yr^{-1} (Fig. 11c), large enough to resolve within the uncertainties of our velocities. In contrast, differences between the vertical and horizontal rates predicted by the TDEFNODE models for maximum locking depth of 35, 40 and 45 km are only 1 mm yr^{-1} or less everywhere in our study area (Fig. 11), close to or below the resolution threshold of our data. The GPS velocities thus have enough information to eliminate a downdip limit of only 25 km for interseismic locking in our study area but are insufficient to discriminate between downdip limits of 35–45 km.

5.2.3 Influence of the RI/CO plate boundary location

Fig. 12 shows how the best-fitting locking solutions vary with the assumed location for the RI/CO plate boundary for a model with a 40-km maximum locking depth and velocities calibrated with τ_m of 15 yr. Independent of the assumed boundary locations, the best-fitting solutions require full locking of the eastern RI/NA trench segment and weak-to-moderate locking of the eastern CO/NA segment (Fig. 12).

The fits to the velocities of sites that are the farthest northwest and southeast in our study area (Figs 12 and 13) and fits to all the vertical velocities (Figs 13c and d) are equally good for all three assumed boundary locations. Those subsets of the velocity field thus cannot discriminate between the alternative RI/CO boundary locations. Instead, the critical subset of our velocities is located along the coast and inland from 105°W to 104°W, at the centre of our study area (Fig. 12). Here, a transition occurs between the onland areas that are above the subducting CO versus the RI plates. The horizontal motions of the stations in the transitional region are fit poorly by the models that were derived using RI/CO locations 1 and 2 within and on the eastern edge of the Manzanillo Trough (Figs 12b and c), but are fit well for the RI/CO boundary location ∼50 km northwest of the Manzanillo Trough (Fig. 12a). The site velocities are thus more consistent with models in which the oceanic lithosphere that subducts beneath the Manzanillo Trough is part of the CO rather than RI plate. Based on the broadly scattered seismicity that occurs outboard from the trench in this transitional area (Fig. 5a), our discrete-boundary assumption is clearly an approximation. The boundary instead more likely includes multiple active faults that accommodate a gradual transition in the plate motion.

5.2.4 Influence of the RI angular velocity with respect to NA

None of our models predict horizontal velocities along the Jalisco segment that are as fast as observed (Section 5.2 and Figs 6 a and 7b), including the solutions with a fully locked subduction interface and locking depth that maximizes the potential locking area (45 km). We thus explored the sensitivity of the misfit F to plausible increases in the assumed RI–NA convergence rate based on the presumption that the interplate convergence rate accelerated during the past 0.78 Myr or is underestimated by the MORVEL 0.78-Myr-average RI–NA angular velocity. We explored angular rates up to 35 per cent faster than the MORVEL angular rate, which has a formal 95 per cent uncertainty equal to ±15 per cent of the 4.37° Myr^{-1} angular rate (defined by the yellow area in Figs 14a–c).

Fig. 14 summarizes the variations in misfit as a function of the assumed mantle Maxwell time and RI/CO boundary locations. We fixed the maximum locking depth to 40-km for these inversions to allow for the maximum potential locking area. Relative to the fit of the best-fitting model identified above ($F = 4.0$ indicated by the solid purple line in Figs 14a–c), 10 of the 147 models that we tested gave superior fits (Figs 14a–c). Four of these ten models have the same characteristics as our preferred model, namely τ_m of 15 yr, a 40-km maximum interface locking depth and an RI/CO plate boundary that intersects the trench ∼50 km northwest of the Manzanillo Trough. The RI–NA angular rates for all four of these models are 20–35 per cent faster than the MORVEL estimate, larger than the 95 per cent upper bound on the MORVEL angular rotation rate.

All six of the remaining models that improved the fit were derived from velocities that were calibrated for a Maxwell time of 40 yr (Figs 14a–c). None of the TDEFNODE models that were derived from velocities calibrated for values of $\tau_m \leq 8$ yr or from velocities that were determined without any calibration for viscoelastic deformation improved on the fit of our preferred model. The latter result reinforces the unsuitability of mantle viscosities less than or equal to 1×10^{19} Pa s for our viscoelastic modelling. All of

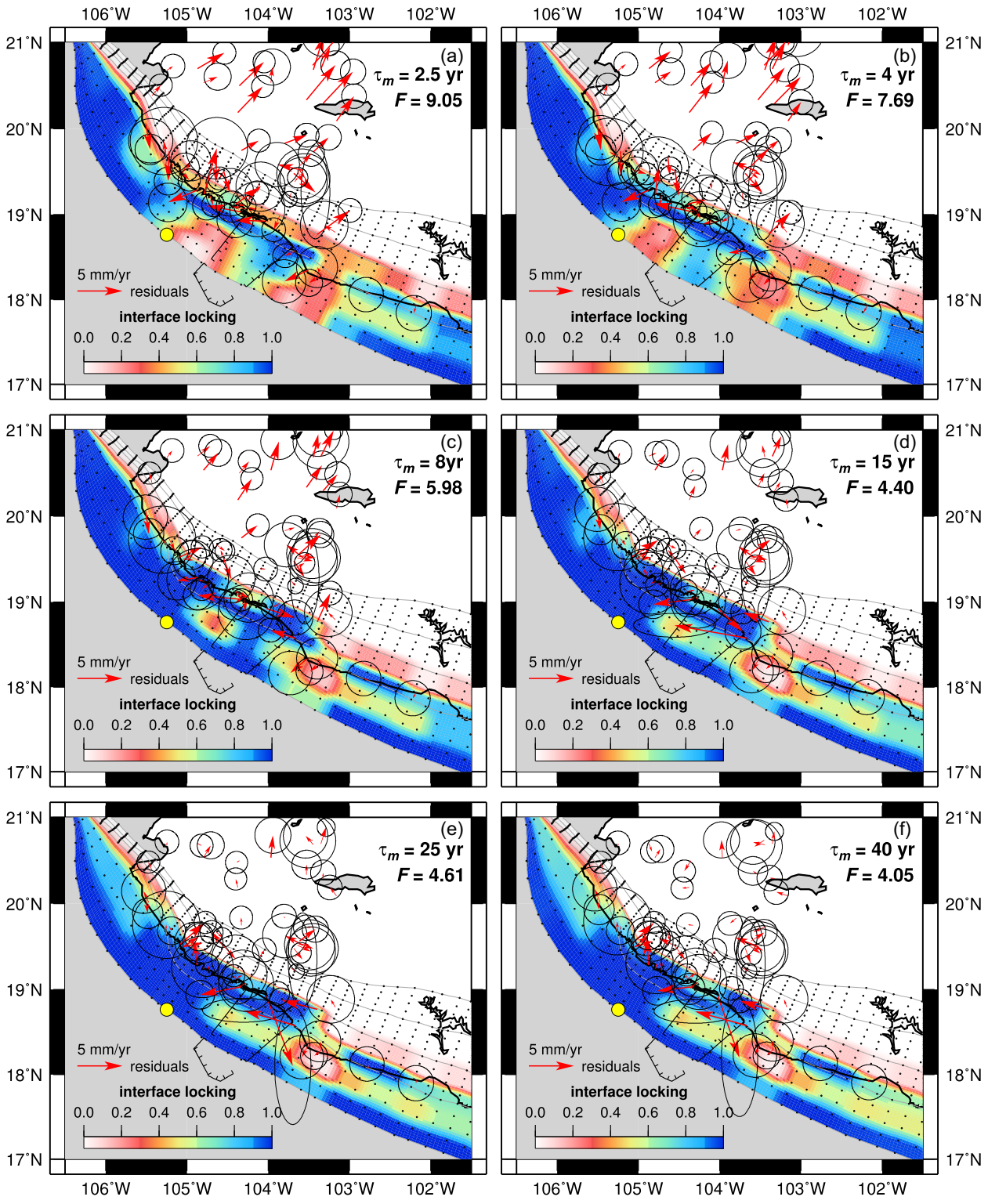

Figure 8. Effect of the viscoelastic corrections for the mantle Maxwell times indicated in each panel. All locking solutions have a maximum permitted locking depth of 40 km and use RI/CO boundary location 3 from Fig. 5. The yellow circles identify the intersection of the RI/CO boundary with the trench. The residual velocities in each panel are the observed minus the velocities predicted by the TDEFNODE inversions described in the text. The velocity ellipses show the estimated 2-D, 1σ uncertainties.

the models with an RI/CO boundary located at position 3 give fits superior to those for the other two boundary locations, reinforcing the evidence that the transition from subducting CO to subducting RI plate occurs northwest of the Manzanillo Trough.

Our exploration of alternative, faster angular rates for the RI–NA plate pair thus identifies two classes of models that could potentially improve the fit to that for our preferred model. If the upper mantle is well approximated using a Maxwell time of 15 yr, then models

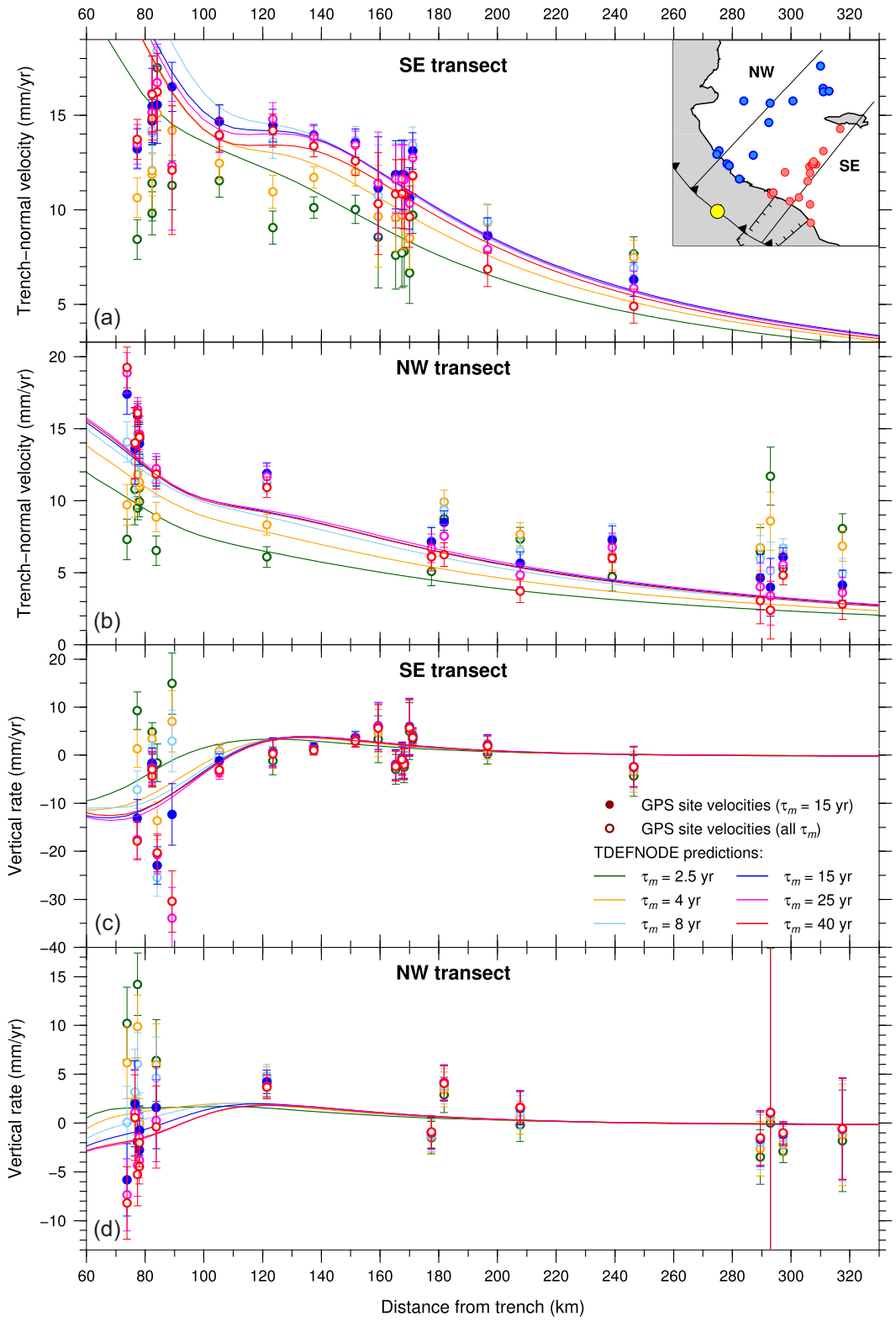

Figure 9. Variation in fits (solid lines) to trench-normal (panels a and b) and vertical (panels c and d) GPS site velocity components with 1σ errors as a function of the assumed mantle Maxwell time denoted by the colours, along the SE (azimuth of N40°E) and NW (azimuth of N45) transects shown on inset. Yellow circle locates the RI/CO boundary.

with RI–NA angular rates that are 20 per cent or more faster than the 0.78-Myr MORVEL estimate are required to improve the fit. If a Maxwell time of 40 yr is more appropriate, then all RI–NA angular rates faster than the MORVEL estimate progressively improve the fit (red symbols in Fig. 14c). Given the similarities of the 15 and 40-yr Maxwell time fits for the time-dependent modelling described in CM21-I, we cannot exclude the possibility that the upper-mantle Maxwell time is closer to 40 than 15 yr.

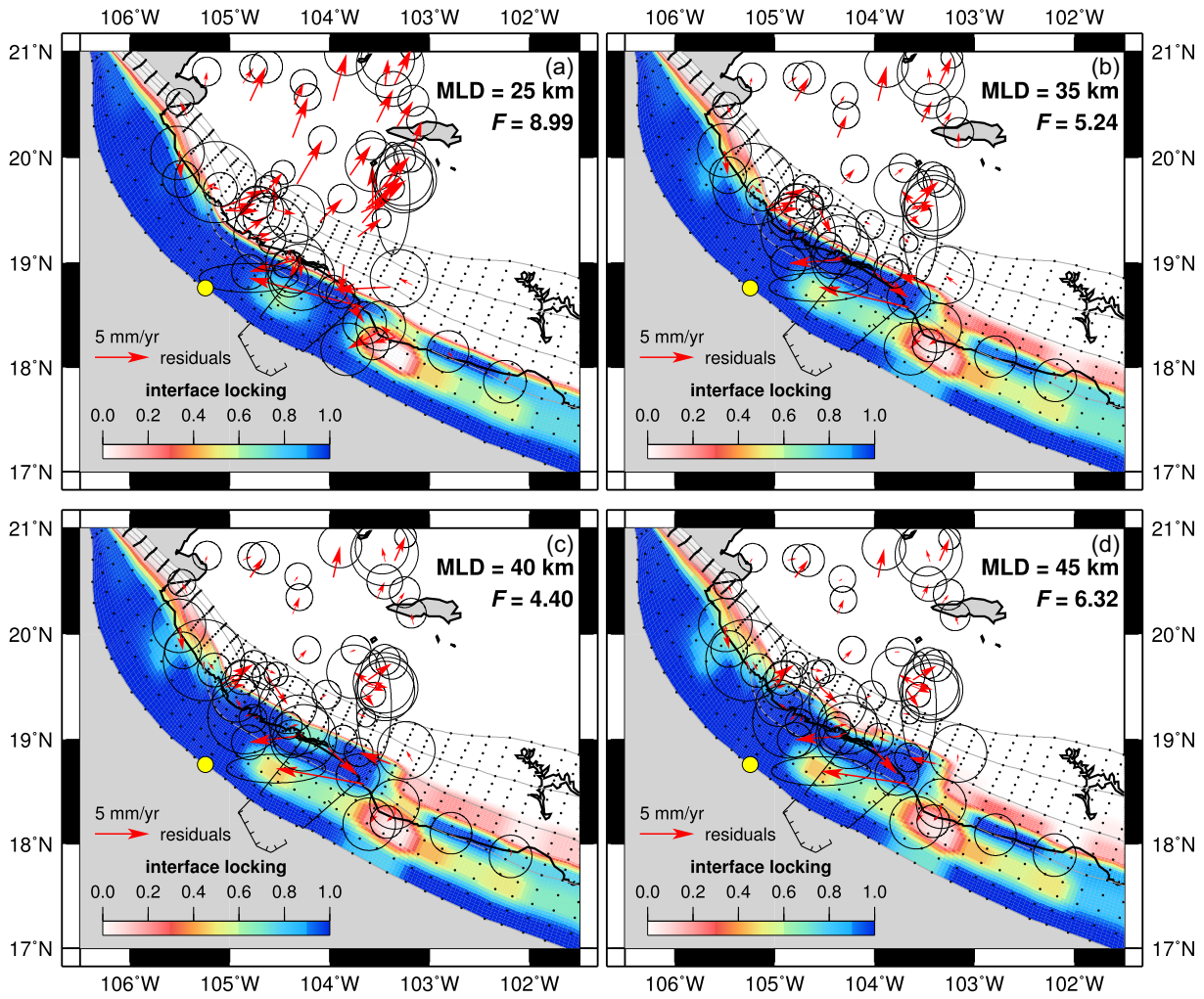

Figure 10. Best-fitting subduction interface locking solutions for the maximum permitted locking depth (MLD) indicated on each panel, assuming τ_m of 15 yr for the viscoelastic velocity field corrections and the RI/CO plate boundary location indicated by the yellow circle in each panel. The residual velocities in each panel are the observed minus the and predicted velocities. The velocity ellipses show the estimated 2-D, 1σ uncertainties.

If the RI–NA America convergence rate has accelerated 20–30 per cent since 0.78 Ma, then enforcing closure of the Pacific–NA–RI plate circuit requires that one or both of Pacific–NA or Pacific–RI plate motion has changed over the same time frame. A comparison of present-day Pacific–NA plate motion determined from GPS to reconstructions of the plate motion during the past 20 Myr reveals no significant change in the plate motion since 4.2 Ma (DeMets & Merkouriev 2016). By implication, a 20–30 per cent acceleration of RI–NA plate convergence requires a post-0.78 Ma change in the Pacific–RI angular velocity. We approximated this change by summing a GPS-derived Pacific–NA angular velocity from (DeMets & Merkouriev 2016) with the MORVEL RI–NA pole and an angular rate 25 per cent faster than the MORVEL estimate. The resulting Pacific–RI angular velocity predicts present-day slip directions along the RI transform fault that are 2–10 degrees anticlockwise from its well-mapped fault trace. This difference is 2–3 times larger than the uncertainties in the azimuths of well-mapped segments of the RI transform fault (DeMets *et al.* 2010).

In summary, a 25 per cent acceleration of RI–NA convergence rates since 0.78 Ma is required in order to improve the fit to the GPS site velocities in our study area if the mantle Maxwell time is 15 yr. This exceeds the 95 per cent upper bound on the MORVEL angular rate for this plate pair and thus seems unlikely. If the mantle Maxwell time is instead 40 yr, then any acceleration of the RI–NA convergence rate since 0.78 Ma improves the fit assuming that the boundary that separates the RI and CO plates is located somewhere northwest of the Manzanillo Trough (red symbols in Fig. 14c). Our analysis is thus permissive of a possible convergence rate acceleration, although it suggests that any such acceleration has been ∼10 per cent or less so as to satisfy closure conditions for the Pacific–RI–NA plate circuit.

5.2.5 Influence of the North America plate geodetic reference frame

The persistent inland-pointing residual velocities at the inland sites in our study area (Figs 8, 10, 12 and 15a indicate that our best-fitting elastic models underestimate the elastic shortening rates at the inland sites even with a fully locked or nearly fully locked RI plate subduction interface. Although the systematic misfits might indicate a problem with our model assumptions, it might instead indicate that the observed rates are systematically too fast. Such a bias could arise from an error in the angular velocity that was used by CM21-I to transform their GPS site positions to an NA plate frame

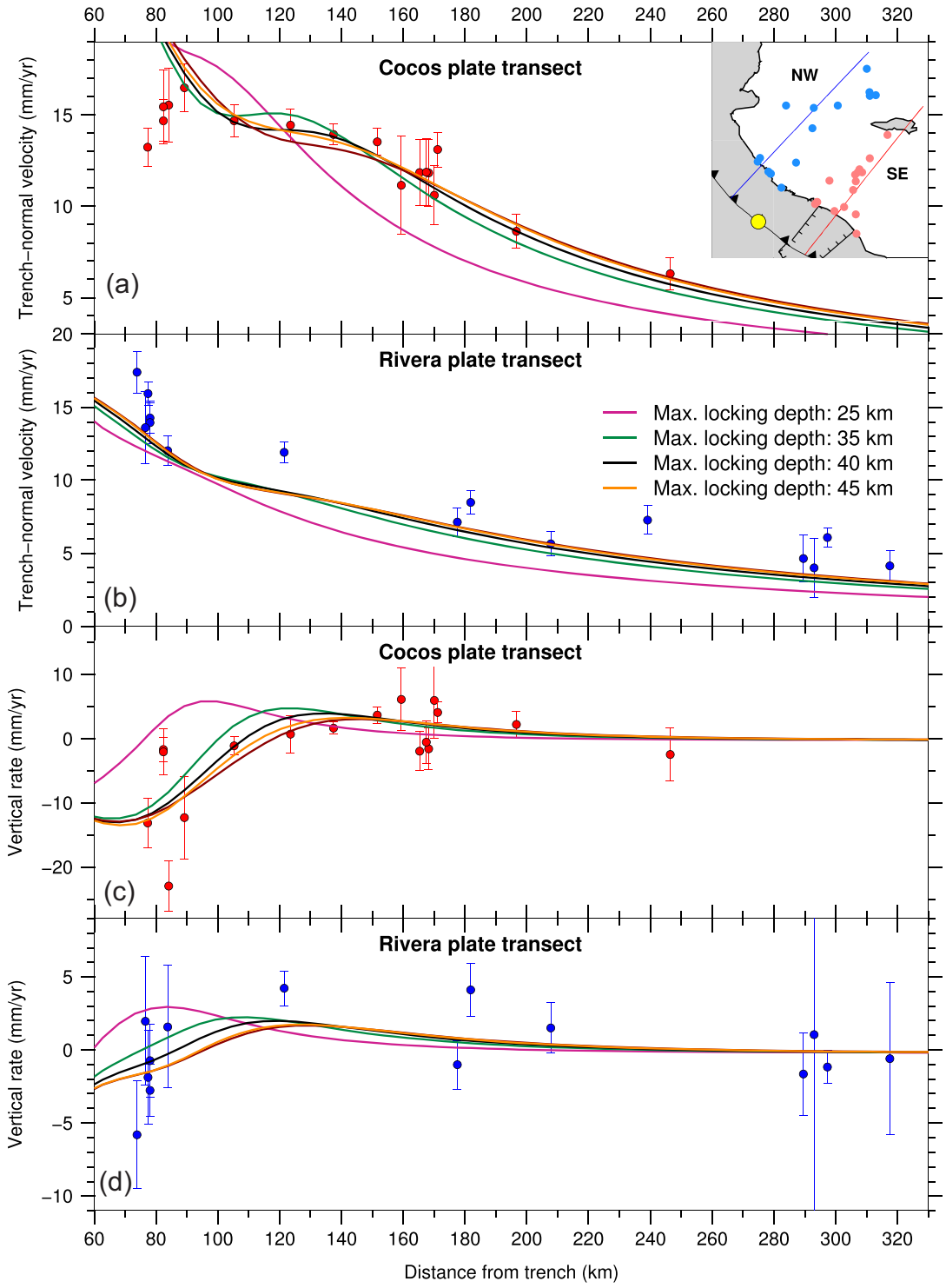

Figure 11. Variation in fits to trench-normal horizontal (panels a and b) and vertical (panels c and d) GPS site velocity components for velocity transects above the RI and CO plates as a function of maximum permitted subduction locking depths from 25 to 45 km. The observed GPS site velocities (red and blue circles) are corrected for viscoelastic effects of the 1995 and 2003 earthquakes assuming $\tau_m = 15$ yr. The predicted velocities (continuous lines) are from the best-fitting TDEFNODE inversions described in the text. The velocity error bars show the estimated 2-D, 1σ uncertainties. Yellow circle shows the assumed location of the RI/CO plate boundary.

of reference. One source for such a bias is the ubiquitous influence on the NA plate velocity field of glacial isostatic adjustments (GIA) due to the loss of continental ice at the end of the last ice age, which is revealed by recent analyses of the NA plate GPS velocity field (Kreemer *et al.* 2018; Ding *et al.* 2019).

From the velocities of more than 3000 continuous GPS stations in Greenland and NA (including much of Mexico), Kreemer *et al.* (2018) find that the IGS08 velocity field is well described by separable components that consist of an NA plate rotation of 2.3°S, 86.0°W, 0.201° Myr^{-1} and plate-wide glacial isostatic deformation that is

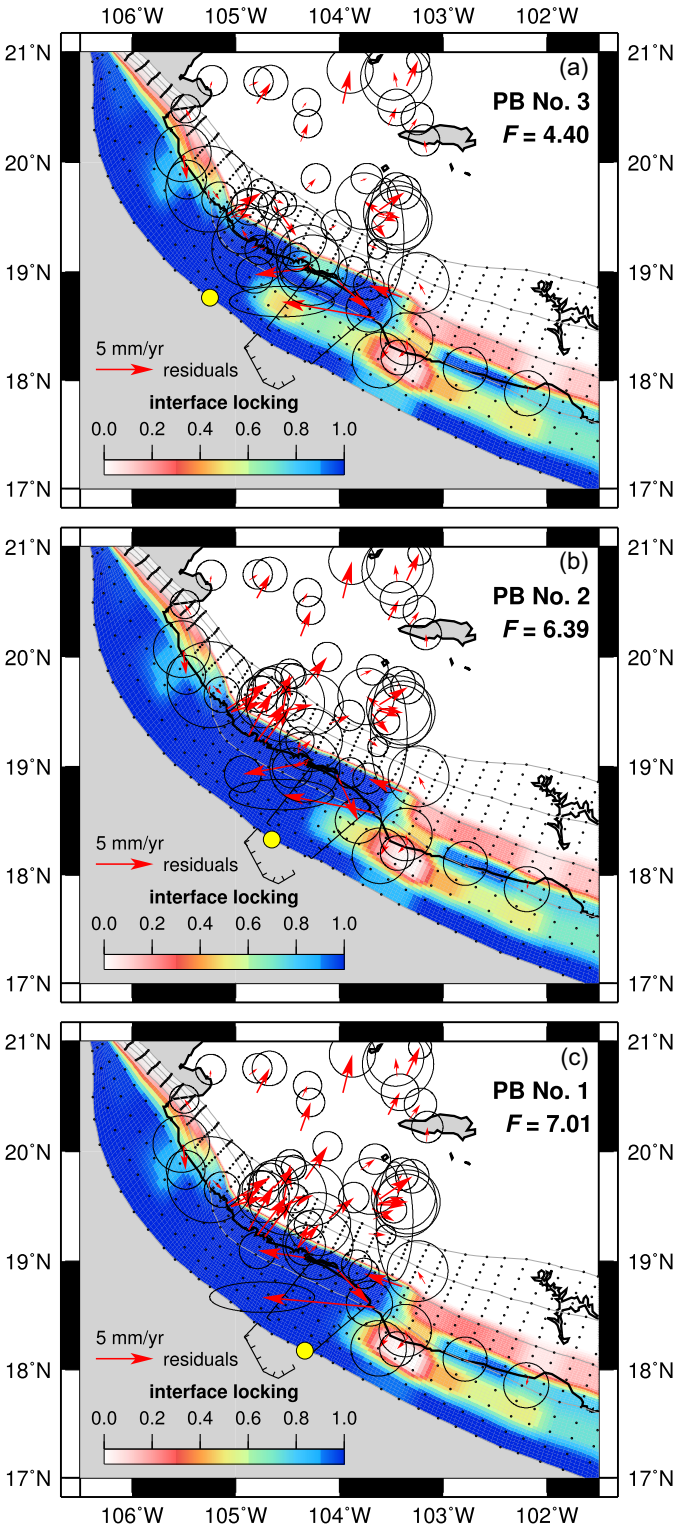

Figure 12. Effect of different assumed RI/CO boundary locations (PB, as labelled in Fig. 5) on subduction interface locking solutions for a maximum permitted locking depth of 40 km and GPS site velocities calibrated assuming a mantle $\tau_m = 15$ yr. The yellow circles identify the intersection of the RI/CO boundary with the trench. The residual velocities in each panel are the observed minus the velocities predicted by the TDEFNODE inversions that are described in the text. The velocity ellipses show the estimated 2-D, 1σ uncertainties.

dominated by contraction towards south-central Canada. At 22.0°N, 100.5°W, ≈350 km east of our study area, the Kreemer *et al.* (2018) results indicate 10.5 mm yr^{-1} towards S58°W of NA plate motion and GIA-induced motion of 2.3 mm yr^{-1} towards N10°W (see their table S3). Their analysis thus requires a net velocity correction of $V_{east} = -9.3$ mm yr^{-1} and $V_{north} = -3.3$ mm yr^{-1} in order to transform GPS site velocities at this location to the Kreemer *et al.* NA plate frame of reference. A similar calculation for a site at 23.0°N,

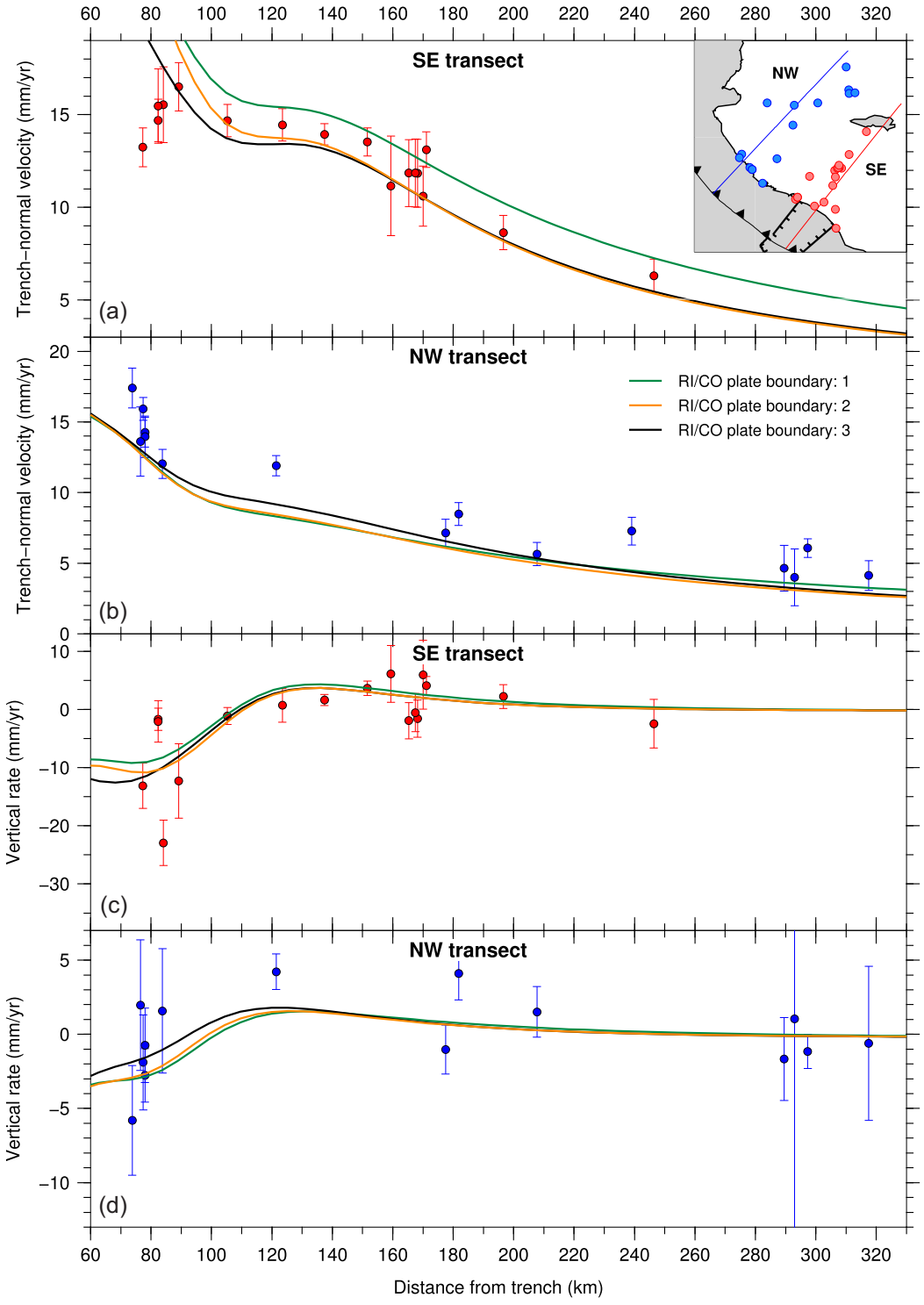

Figure 13. Variation in fits to trench-normal horizontal (panels a and b) and vertical (panels c and d) GPS site velocity components for transects above the RI and CO plates as a function of the location of the RI/CO plate boundary. GPS site velocities are corrected for viscoelastic effects of the 1995 and 2003 earthquakes assuming $\tau_m = 15$ yr. The predicted velocities are from the best-fitting TDEFNODE inversions described in the text. The velocity error bars show the estimated 2-D, 1σ uncertainties.

102.5°W, ≈350 km north of our study area gives a net velocity correction of $V_{east} = -10.0$ mm yr^{-1} and $V_{north} = -3.2$ mm yr^{-1}, including 3.2 mm yr^{-1} towards N14°W of GIA-induced motion.

At the same two sites, the angular velocity we used in our CM21-I analysis to transform GPS site positions to an NA frame of reference, 7.45°S, 87.96°W, 0.183° Myr^{-1}, predicts east and north velocity components of $V_{east} = -9.8$ mm yr^{-1} and $V_{north} = -4.4$ mm yr^{-1} at the eastern site and $V_{east} = -10.1$ mm yr^{-1} and $V_{north} = -5.1$ mm yr^{-1} at the northern site. The CM21-I angular velocity however ignores the plate-wide effects of GIA on the GPS site velocities that were used in its estimation. The vector differences between the net velocity corrections based on the Kreemer *et al.* (2018)

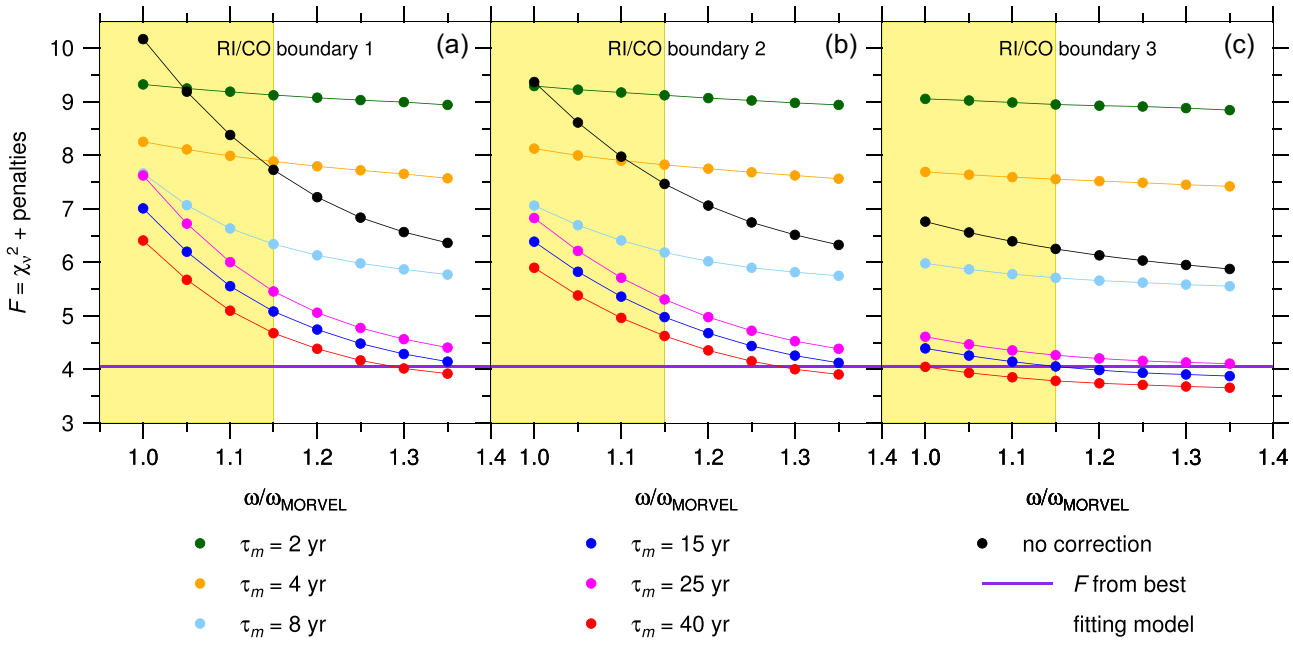

Figure 14. Influence of the RI–NA plate angular rotation rate on the misfit F for TDEFNODE inversions of GPS velocities in our study area. The RI–NA angular rotation rates ω are expressed as a fraction of the 4.37° Myr^{-1} RI–NA angular rate (ω_{MORVEL}) from the global plate motion model MORVEL (DeMets *et al.* 2010). GPS velocities are inverted while imposing a 40 km maximum interface locking depth and for the three alternative locations for the RI/CO plate boundary that are defined in Fig. 5(a). Misfits are shown for inversions of GPS velocities that are calibrated for all six mantle Maxwell times τ_{m} specified in the legend and for velocities without any viscoelastic calibration. The yellow region in each figure encompasses the 95 per cent uncertainty interval for the MORVEL RI–NA angular rotation rate. The violet line denotes the F value of our preferred model, that is the model with a 40-km maximum interface locking depth, $\tau_{\mathrm{m}} = 15$ yr, and RI/CO boundary location ∼50 km NW of the Manzanillo Trough (see the text).

results and those estimated with the CM21-I angular velocity thus closely approximate the likely systematic bias in the CM21-I NA plate velocity estimate in and near our study area. Specifically, at the eastern and northern sites that are defined in the previous paragraph, the velocity corrections that are required to transform GPS results to the Kreemer *et al.* (2018) NA plate frame of reference are respectively 1.2 and 1.8 mm yr^{-1} slower than but in nearly the same direction as the velocity corrections that are estimated with the CM21-I NA plate angular velocity.

Based on the above, the GPS site velocities that we used for our analysis are 1.2 to 1.8 mm yr^{-1} too fast but in the correct direction relative to the Kreemer *et al.* (2018) geodetic definition of the NA plate frame of reference. This difference is consistent with the 0.5–3 mm yr^{-1} N-NNE-directed misfits at most of our inland sites (black arrows in Fig. 15b). Averaging the individual station misfits in order to better identify the common component of the misfits yields even better agreement: the 1.2 mm yr^{-1}, N26°E average misfit (the blue arrow in Fig. 15b) differs from the apparent reference frame velocity bias by only 0–0.6 mm yr^{-1}. A comparison of the trench-normal site velocities in Fig. 13b to the velocities estimated with our preferred model clearly shows that reducing all the GPS velocities by 1.2–1.8 mm yr^{-1} would more closely align the observed and modelled velocities.

We conclude that the inland-directed misfits at most of the inland stations are consistent with a small but significant bias in our definition of the NA plate frame of reference. Similar misfits at the inland sites for the 8 and 25-yr Maxwell times (Figs 15 c and d), which bracket our preferred 15-yr Maxwell time, would also be reduced in the Kreemer *et al.* (2018) NA plate frame of reference. Reducing the trench-normal velocity components of the GPS sites in Jalisco by 1.2–1.8 mm yr^{-1} would improve the fits of the preferred model (Fig. 6a) to the site velocities nearly everywhere above the RI plate (Figs 7b and 13b). A GIA correction to our estimated site velocities would thus reinforce the evidence for strong locking of the RI plate subduction interface.

6 DISCUSSION

6.1 Earthquake cycle implications for the Jalisco/Colima/Michoacán trench segments

Our new interseismic locking solution, which is constrained by GPS station velocities that extend to the northwesternmost limit of the Mexico subduction zone, indicates that strong locking extends to the northwest limit of the trench, including a region of the interface that has not ruptured since 1932 (Fig. 6a). For an average annual elastic slip deficit of ∼20 mm yr^{-1} (Fig. 6b), ∼1.8 m of unrelieved interface slip has accumulated since 1932, sufficient to cause an $M > 7$ earthquake depending on the lateral and downdip extent of the future earthquake. If the entire interface northwest of the 1995 Colima–Jalisco earthquake zone ruptured in one earthquake, comprising a potential rupture area of ∼15 500 km^2, the release of the accumulated slip deficit would produce an M∼8 earthquake. Elsewhere in our study area, the annual slip-rate deficits range from as little as ∼10 to ∼60 mm yr^{-1} (Fig. 6b), sufficient to generate $M \sim 7$ or larger earthquakes at least once per century. The hazards from subduction thrust earthquakes are thus significant everywhere in our study area, including the areas of weak-to-moderate interface locking east of the Manzanillo Trough.

Pacheco *et al.* (1993) suggest that variations in seismic coupling are associated with differences in frictional behaviour along the subduction interface, which may be caused by the subduction of

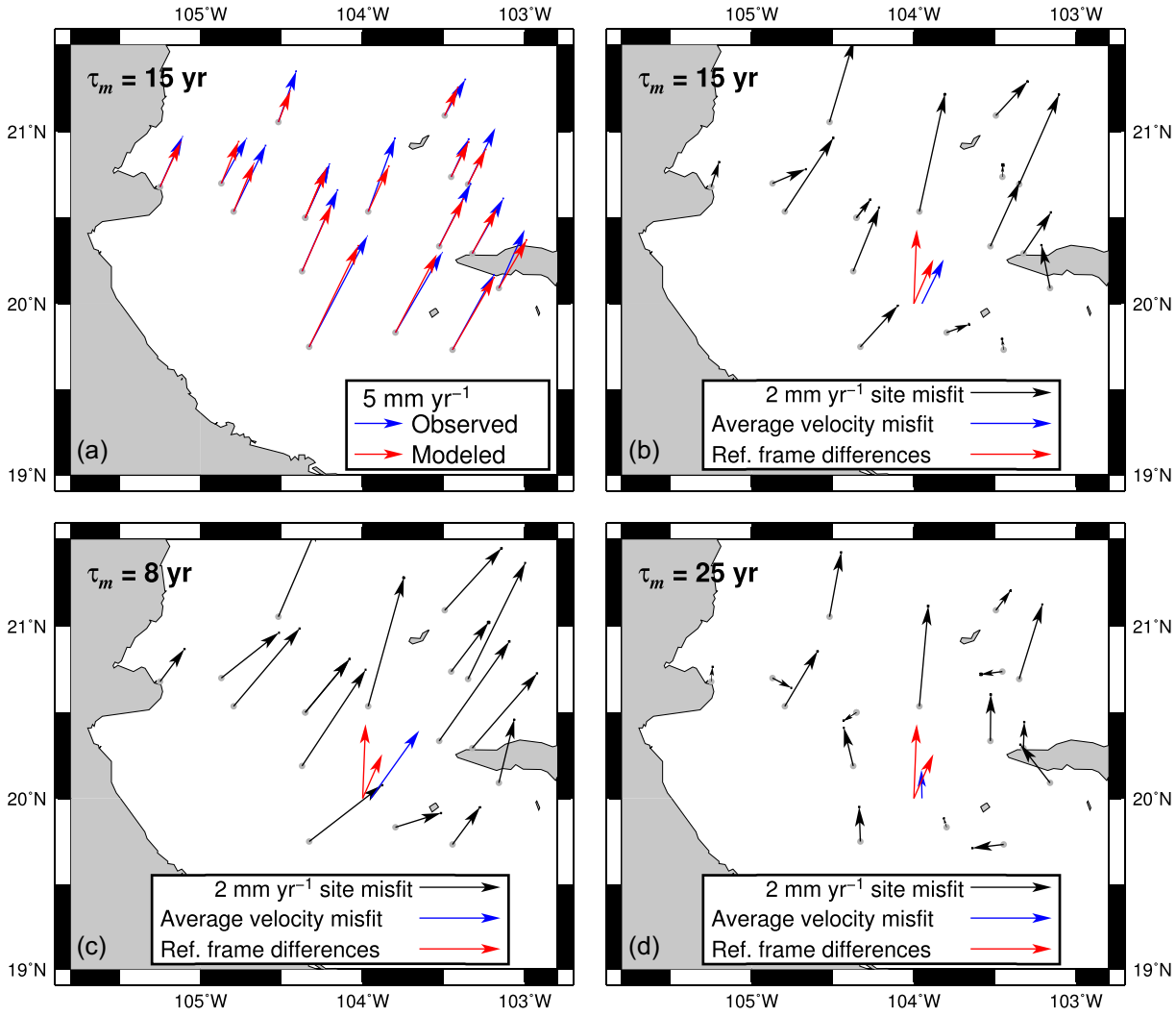

Figure 15. Influence of the geodetic reference frame realization on the interpretations of GPS site velocity misfits for three best-fitting elastic models estimated in the analysis. (a) Observed GPS site velocities from Fig. 2a (blue arrows) and velocities estimated with our best-fitting elastic model (red arrows) for an assumed mantle Maxwell time of 15 yr. The site motions are with respect to the NA plate interior, whose motion was estimated from the velocities of ∼1000 GPS sites that are located outside the region of rapid post-glacial adjustments. (b) Observed-minus-modelled site velocities from panel (a) (black arrows) and the average velocity misfit for all 16 GPS sites (blue arrow) compared to the differential movements (red arrows) at two locations near our study area (see the text) of a plate-centric frame of reference that accounts for the rotation of the NA plate and far-field effects of glacial isostatic adjustments in NA (Kreemer *et al.* 2018) versus the undeforming plate-centric frame used for our analysis (see the text). The similarity of the averaged velocity misfits and differential reference frame velocity suggests that the misfits may be an artefact of a possible ∼1 mm yr^{-1} SW-directed bias in the frame of reference that we used for our analysis. Panels (c) and (d) repeat the information from panel (b) but for velocity fields and best-fitting elastic models based on alternative mantle Maxwell times of 8 and 25 yr, respectively. Stations near the trench are excluded from the comparison because their velocities and misfits are strongly influenced by the near-field effects of spatial variations in locking on the subduction interface.

large bathymetric features, the presence of unstable triple junctions, sediment composition and other factors. The most robust feature of our locking solutions, namely the along-strike change from weak locking southeast of the Manzanillo Trough to strong locking northwest of the trough (Fig. 6a), coincides well with the limits of the 1932, 1973, 1995 and 2003 earthquake rupture zones and afterslip after the latter two earthquakes (Figs 1 and 16). The along strike transition from strong to patchier locking (Fig. 16) is also located directly updip from an along-strike gap in non-volcanic tremor identified by Brudzinski *et al.* (2016). Together, these suggest that the Manzanillo Trough may be a mechanical barrier for along-strike rupture propagation (e.g. Schmitt *et al.* 2007), and may mark a transition in the physical or possibly kinematic properties that affect the frictional behaviour of the subduction interface.

Our interplate locking solution for the northernmost ∼500 km of the Mexico subduction zone and the Rousset *et al.* (2015) interseismic locking solution for the ∼700-km-long Guerrero and Oaxaca trench segments that extend east from our study area collectively reveal multiple significant along-strike variations in the locking of the CO and RI plate subduction interfaces at depths above 25 km. These variations include alternating areas with locking greater than 0.7 and areas with locking less than 0.3. Within our study area, the only significant along-strike variation in locking is located near the Manzanillo Trough, an upper plate structural discontinuity that may coincide with a transition from subducting CO to RI plate oceanic lithosphere. In contrast, Rousset *et al.* (2015) find a strong spatial correlation between trench-to-coast distance and regions of strong versus weak shallow coupling for the Guerrero and Oaxaca

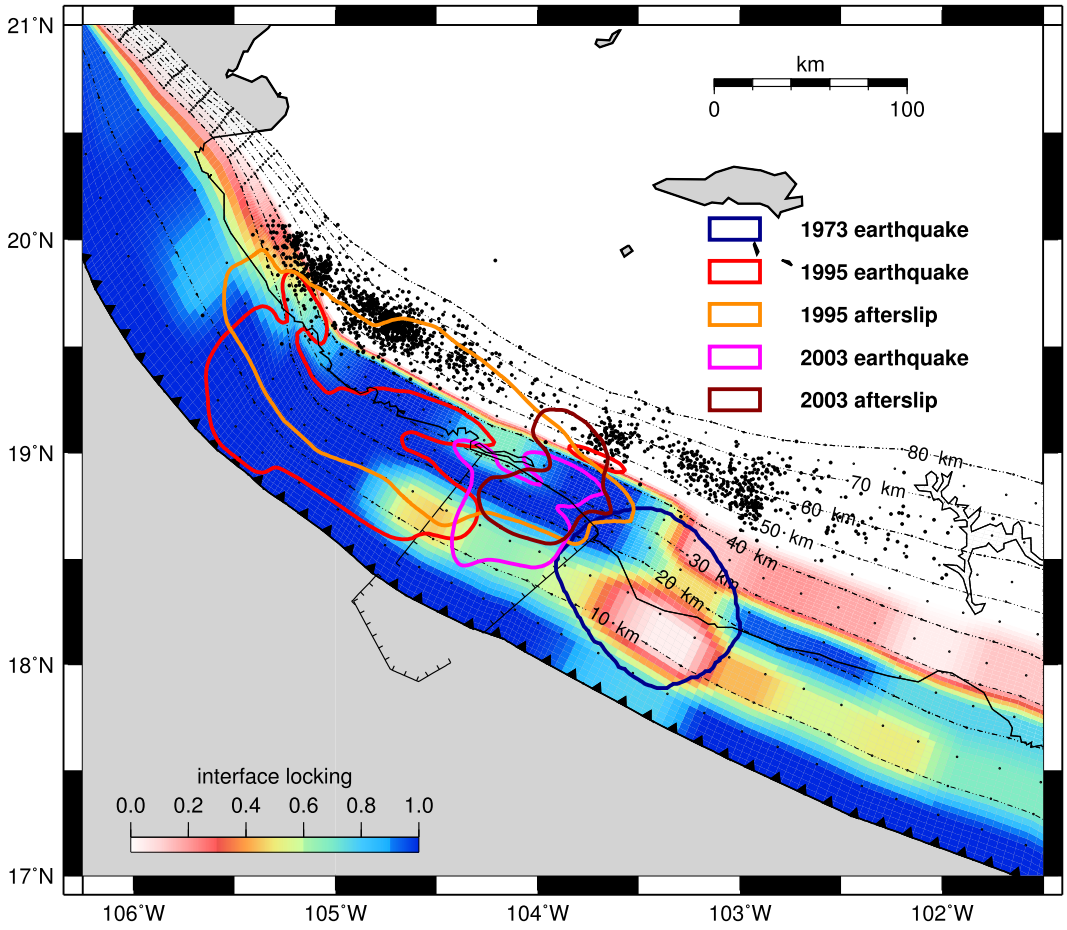

Figure 16. Locations of recent large thrust earthquakes (1973: blue; 1995: red; 2003: magenta), afterslip (1995: orange; 2003: dark red) and non-volcanic tremor (black dots) along the Jalisco–Colima subduction interface superposed to our preferred locking solution. The 1973 rupture is from Reyes *et al.* (1979). The 1995 and 2003 co-seismic ruptures and afterslip correspond to the 0.5 m contour of the co-seismic slip and afterslip solutions from a model with viscoelastic rebound corrections using $\tau_m = 15$ yr (CM21-I). Tremor locations are from Brudzinski *et al.* (2016).

segments, which they attribute to along-strike variations in the mechanical properties of the upper plate. A single explanation for the lateral locking variations along the entire subduction zone is thus unclear and beyond the scope of this work.

Non-volcanic tremor in our study region occurs at depths of ∼40–70 km, only ∼10 km farther downdip from the deepest extents of interseismic locking and co-seismic slip in 1995 and 2003 (Fig. 16). If slow slip events (SSE) originate on the interface in the region between non-volcanic tremor and co-seismic slip, as may be the case along the Oaxaca segment (Brudzinski *et al.* 2010), then relatively little of the subduction interface may have the appropriate frictional conditions for slow slip events with amplitudes large enough to be detected with GPS, as suggested by Brudzinski *et al.* (2016). Another possibility is that the large magnitude of post-seismic afterslip at the interface from the 1995 and 2003 earthquakes discourages the occurrence of resolvable SSE, as suggested by numerical models of Nankai (Shi *et al.* 2020). Better GPS coverage in the state of Michoacán and in western Guerrero, where security is a concern, is needed to determine if slow slip events offshore from or beneath the state of Michoacán relieve a significant fraction of the accumulating interseismic strain. If they do, they may explain the apparently weaker locking along this segment of the trench.

6.2 Model misfits and sensitivities

The most persistent misfit in the models we tested was to the velocities of sites located in the coastal and inland areas directly inland from the Jalisco segment, where the site velocities were 1–2 mm yr^{-1} faster than predicted by any of our models (Figs 7b, 11b and 12b). The misfits have at least three possible explanations. They may be evidence for an error and/or oversimplification in one or more assumptions that are implicit in our time-dependent modelling, which are discussed at length by CM21-I. Alternatively, they may be evidence for a systematic bias in the far-field plate tectonic constraints that are implicit in this analysis, including our assumption that the 0.78-Myr-average MORVEL RI–NA angular velocity accurately describes the present-day relative motion between these two plates (Section 5.2.4) and/or our assumption that glacial isostatic effects can be neglected to estimate the NA plate angular velocity (Section 5.2.5). To first order, correcting our GPS site velocities for an estimated 1–2 mm yr^{-1} bias related to the plate-wide and localized effects of GIA in our study area would reduce the systematic misfits at our inland sites by half or more (Fig. 15b–d). It would not alter our conclusion that locking of the RI subduction interface is strong, mainly because the locking magnitude is

more sensitive to the velocities of the coastal stations proximal to the locked interface than to the velocities of the remote inland sites.

The largest sensitivity in our locking solutions is associated with the location that is assigned to the intersection of the poorly understood RI/CO plate boundary with the trench. This location determines the *a priori* rate of interplate convergence that is applied to each node on the subduction interface, which in turn constrains the magnitude of the interseismic locking required to fit the nearby GPS site velocities. Our modelling shows that the CO plate subducts rapidly enough to match and/or exceed the onshore surface deformation even for partial locking of the interface. In contrast, full locking of most of the RI/NA interface is required to match the GPS-measured surface velocities in areas above the more slowly subducting RI plate. Models in which the offshore RI/CO plate boundary intersects the trench northwest of the Manzanillo Trough fit our velocities more successfully because larger areas of the subduction interface are driven by faster CO plate subduction and thus fit the measured surface deformation even under conditions of partial coupling. Although the offshore RI/CO plate boundary is more likely to be diffuse than discrete, approximating a diffuse boundary in our elastic model would require hard-to-justify assumptions, the introduction of new hard-to-resolve parameters associated with the newly introduced diffuse boundary, and additional tradeoffs between the new and existing model parameters that we suspect would degrade our estimates of the latter.

7 CONCLUSIONS

We inverted GPS station velocities derived from nearly 25 yr of GPS measurements onshore from the northern ∼500 km of the Mexico subduction zone to estimate an interseismic locking solution for this region (Fig. 6a). Our preferred model requires an average of ∼70 per cent interseismic locking between the surface and depths of 40 km, non-uniformly distributed along the interface. The most robust features of the locking solution are:

(i) Transitions along the trench from strong locking (>90 per cent) of the Jalisco segment subduction interface at depths shallower than ∼20 km to moderate-to-strong locking (average of ∼80 per cent) of the Colima segment below the Manzanillo Trough to weak-to-moderate locking (average ∼55 per cent) of the CO/NA subduction interface southeast of the Manzanillo Trough (Michoacán segment).

(ii) Strong locking of the subduction interface to depths of 40 km along the trench segments ruptured by the 1995 Colima–Jalisco and 2003 Tecomán thrust earthquakes, at depths where afterslip relieved significant accumulated elastic strain after both earthquakes.

(iii) Evidence that elastic strain that has accumulated along the ∼125-km-long trench segment offshore from Puerto Vallarta and other developed coastal areas, where the last large thrust earthquake occurred in 1932, is sufficient to release an M∼8.0 earthquake if all of the stored elastic energy was released simultaneously.

These features are robust with respect to mantle Maxwell times of 15, 25 and 40 yr, which give rise to the lowest misfits. They are also robust with respect to variations in the maximum depth that is permitted for interseismic locking and the location where the poorly understood RI–CO plate boundary is assumed to intersect the trench. The relatively small 1.2 mm yr^{-1} north and 1.1 mm yr^{-1} east GPS velocity component misfits for our preferred model suggest that most of our model assumptions, including the linear viscoelastic rheology we use for the upper mantle, are adequate. We interpret a 1–2 mm yr^{-1} systematic misfit to the subset of our data located above the subducting RI plate as evidence that one or more of our modelling assumptions require refinements, including a possible acceleration of RI/NA convergence rates since 0.78 Ma or a correction for the effects of glacial isostatic rebound on our estimate of the NA plate angular velocity, which serves as a frame of reference for this study. Future refinements in estimates of NA plate motion that are corrected for the effects of glacial isostatic rebound would clearly benefit tectonic and earthquake hazard studies in our study area and other parts of the Mexico subduction zone.

The mantle viscosity that gives the best overall fit for both the time-dependent and static modelling in our two stage analysis, 2 × 10^{19} Pa s, is similar to viscosities estimated in previous studies, including 3.2 × 10^{19} Pa s (τ_m = 20 yr, μ = 50 GPa) for the 1964 Alaska earthquake (Suito & Freymueller 2009), viscosities of the order of 10^{19} Pa s for the 1960 Chile, 2006 Sumatra and ∼1700 Cascadia megathrust earthquakes (Wang *et al.* 2012), 0.5 × 10^{19} Pa s and 3 × 10^{19} Pa s respectively for a low-viscosity wedge and the long-term mantle viscosity (Trubienko *et al.* 2013), and 0.8–1.5 × 10^{19} Pa s (8 yr $\leq\tau_m \leq$ 15 yr, μ = 30 GPa), from modelling of long-term post-seismic deformation in Nankai (Johnson & Tebo 2018).

ACKNOWLEDGEMENTS

We thank Jeffrey Freymueller, an anonymous reviewer and the associate editor for constructive suggestions. Support for this work during its various stages was provided by NSF grants EAR-9526419, EAR-9804905, EAR-9909321, EAR-0510553 and EAR-1114174; and the University of Wisconsin-Madison. This material is based on GPS data and services provided by the GAGE Facility, operated by UNAVCO, Inc. and by the TLALOCNet GPS network operated by Servicio de Geodesia Satelital (SGS; Cabral-Cano *et al.* 2018) at the Instituto de Geofísica-Universidad Nacional Autónoma de México (UNAM). UNAVCO's initial support for TLALOCNet (now part of NOTA) was performed under EAR-1338091 and is currently supported by the National Science Foundation and the National Aeronautics and Space Administration under NSF Cooperative Agreement EAR-1724794. TLALOCNet and other GPS related operations from SGS have also been supported by the Consejo Nacional de Ciencia y Tecnología (CONACyT) projects 253760, 256012 and 2017-01-5955, UNAM-Programa de Apoyo a Proyectos de Investigación e Innovación Tecnológica (PAPIIT) projects IN104213, IN111509, IN109315-3, IN104818-3, IN107321 and supplemental support from UNAM-Instituto de Geofísica. We are deeply grateful to all personnel from UNAVCO and SGS for station maintenance, data acquisition, IT support and data curation and distribution for these networks and in particular to the following individuals and institutions, whose hard work and resourcefulness were central to the success of this project: Bill Douglass, Neal Lord and Bill Unger at UW-Madison, Oscar Díaz-Molina and Luis Salazar-Tlaczani at SGS, John Galetzka, Adam Wallace, Shawn Lawrence, Sean Malloy and Chris Walls at UNAVCO, Jesus Pacheco-Martínez at Universidad Autónoma de Aguascalientes, personnel at the Universidad de Guadalajara at campus Guadalajara, Mascota and Ameca, Protección Civil de Jalisco, Universidad de Colima at campus Colima and campus El Naranjo, and Instituto de Biología-UNAM Estación Chamela. Most figures were produced using Generic Mapping Tools software (Wessel & Smith 1991).

DATA AVAILABILITY

The raw GPS data that are the foundation of the velocity fields used for our analysis are in the public domain and available at http://unavco.org, with the exception of sites COLI and INEG. Data from the GPS sites COLI and INEG for the period 1993–2001 were provided courtesy of Professor Bertha Márquez-Azúa of the University of Guadalajara (bmarquez@cencar.udg.mx). COLI and INEG data from 2001 to 2020 were procured from ftp://geodesia.inegi.org.mx. The individual data set DOIs for the raw GPS time-series are referenced in CM21-I. The velocity fields used for this analysis are provided in the Supplementary Information for CM21-I.

REFERENCES

Alvarez, R. & Yutsis, V., 2015. The elusive Rivera-Cocos plate boundary: not diffuse, in *Magmatic Rifting and Active Volcanism,* Vol. 420, eds Wright, T.J., Ayele, A., Ferguson, D.J., Kidane, T. & Vye-Brown, C., Geological Society.

Bandy, W., Mortera-Gutiérrez, C., Urrutia-Fucugauchi, J. & Hilde, T.W.C., 1995. The subducted Rivera-Cocos plate boundary: where is it, what is it, and what is its relationship to the Colima rift? *Geophys. Res. Lett.,* **22,** 3075–3078.

Bandy, W.L. *et al.*, 2005. Subsidence and strike-slip tectonism or the upper continental slope off Manzanillo, Mexico, *Tectonophysics,* **398,** 115–140.

Bandy, W.L., Kostoglodov, V. & Mortera-Gutiérrez, C.A., 1998. Structure of the southern Jalisco subduction zone, Mexico, as inferred from gravity and seismicity, *Geofis. Int.,* **3,** 153–169.

Brudzinski, M., Schlanser, K.M., Kelly, N.J., DeMets, C., Grand, S.P., Márquez-Azua, B. & Cabral-Cano, E., 2016. Tectonic tremor and slow slip along the northwestern section of the Mexico subduction zone, *Earth planet. Sci. Lett.,* **454,** 259–271.

Brudzinski, M.R., Hinojosa-Prieto, H.R., Schlanser, K.M., Cabral-Cano, E., Arciniega-Ceballos, A., Díaz-Molina, O. & DeMets, C., 2010. Nonvolcanic tremor along the Oaxaca segment of the Middle America subduction zone, *J. geophys. Res.,* **115,** B00A23, doi:10.1029/2008JB006061.

Cabral-Cano, E., *et al.* 2018. TLALOCNet: A continuous GPS-Met backbone in Mexico for seismotectonic and atmospheric research, *Seismol. Res. Lett.,* **89**(), 373–381, doi: 10.1785/0220170190.

Cosenza-Muralles, B., DeMets, C., Márquez-Azúa, B., Sánchez, O., Stock, J., Cabral-Cano, E. & McCaffrey, R., 2021. Coseismic and postseismic deformation for the 1995 Colima–Jalisco and 2003 Tecomán thrust earthquakes, Mexico subduction zone, from modelling of GPS data, *Geophys. J. Int.*. Available at: https://doi.org/10.1093/gji/ggab435.

DeMets, C., Carmichael, I., Melbourne, T., Sanchez, O., Stock, J., Suarez, G. & Hudnut, K., 1995. Anticipating the successor to Mexico's largest historical earthquake, *EOS, Trans. Am. geophys. Un.,* **76**(42), 417–424.

DeMets, C., Gordon, R.G. & Argus, D.F., 2010. Geologically current plate motions, *Geophys. J. Int.,* **181,** 1–80.

DeMets, C. & Merkouriev, S., 2016. High-resolution reconstructions of Pacific-North America plate motion: 20 Ma to present, *Geophys. J. Int.,* **207,** 741–773.

DeMets, C. & Stein, S., 1990. Present-day kinematics of the Rivera plate and implications for tectonics in southwestern Mexico, *J. geophys. Res.,* **95**(B13), 21 931–21 948.

DeMets, C. & Wilson, D.S., 1997. Relative motions of the Pacific, Rivera, North American, and Cocos plates since 0.78 Ma, *J. geophys. Res.,* **102,** 2789–2806.

Ding, K., Freymueller, J.T., He, P., Wang, Q. & Xu., C., 2019. Glacial isostatic adjustment, intraplate strain, and relative sea level changes in the eastern United States, *J. geophys. Res.,* **124,** 6056–6071.

Hutton, W., DeMets, C., Sanchez, O., Suarez, G. & Stock, J., 2001. Slip kinematics and dynamics during and after the 1995 October 9 Mw=8.0 Colima–Jalisco earthquake, Mexico, from GPS geodetic constraints, *Geophys. J. Int.,* **146,** 637–658.

Johnson, K.M. & Tebo, D., 2018. Capturing 50 years of postseismic mantle flow at Nankai subduction zone, *J. geophys. Res.,* **123,** 10091–10106.

Kreemer, C., Hammond, W. C. & Blewitt, G., 2018. A robust estimation of the 3-D intraplate deformation of the North America plate from GPS, *J. geophys. Res.,* **123,** 4388–4412.

Marquez-Azua, B., DeMets, C. & Masterlark, T., 2002. Strong interseismic coupling, fault afterslip, and viscoelastic flow before and after the Oct. 9, 1995 Colima–Jalisco earthquake: continuous GPS measurements from Colima, Mexico, *Geophys. Res. Lett.,* **29,** doi:10.1029/2002GL014702.

Martínez-López, M.R. & Mendoza, C., 2016. Acoplamiento sismogénico en la zona de subducción de Michoacán-Colima–Jalisco, México, *B. Soc. Geol. Mex.,* **68**(2), 199–214.

McCaffrey, R., 2002. Crustal block rotations and plate coupling, in *Plate Boundary Zones,* Vol. 30, pp. 101–122, eds Stein, S. & Freymueller, J.T, American Geophysical Union.

McCaffrey, R., 2005. Block kinematics of the Pacific-North America plate boundary in the southwestern United States from inversion of GPS, seismological, and geologic data, *J. geophys. Res.,* **110,** B07401, doi:10.1029/2004JB003307.

Melbourne, T., Carmichael, I., DeMets, C., Hudnut, K., Sanchez, O., Stock, J., Suarez, G. & Webb, F., 1997. The geodetic signature of the M8.0 Oct. 9, 1995, Jalisco subduction earthquake, *Geophys. Res. Lett.,* **24,** 715–718.

Melbourne, T.I., Webb, F.H., Stock, J.M. & Reigber, C., 2002. Rapid postseismic transients in subduction zones from continuous GPS, *J. geophys. Res.,* **107**(B10), 2241, doi:10.1029/2001JB000555.

Okada, Y., 1985. Surface deformation to shear and tensile faults in a half-space, *Bull. seism. Soc. Am.,* **75,** 1135–1154.

Pacheco, J.F., Sykes, L.R. & Scholz, C.H., 1993. Nature of seismic coupling along simple plate boundaries of the subduction type, *J. geophys. Res.,* **98, B8,** 14 133–14 159.

Pardo, M. & Suárez, G., 1995. Shape of the subducted Rivera and Cocos plates in southern Mexico: Seismic and tectonic implications, *J. geophys. Res.,* **100**(B7), 12 357–12 373.

Reyes, A., Brune, J.N. & Lomnitz, C., 1979. Source mechanism and aftershock study of the Colima, Mexico earthquake of January 30, 1973, *Bull. seism. Soc. Am.,* **69,** 1819–1840.

Rousset, B. *et al.*, 2015. Lateral variations of interplate coupling along the Mexican subduction interface: relationships with long-term morphology and fault zone mechanical properties, *Pure appl. Geophys.,* **172**(12), 3265–3670.

Savage, J.C., 1983. A dislocation model of strain accumulation and release at a subduction zone, *J. geophys. Res.,* **88,** 4984–4996.

Schmitt, S.V., DeMets, C., Stock, J., Sanchez, O., Marquez-Azua, B. & Reyes, G., 2007. A geodetic study of the 2003 January 22 Tecomán, Colima, Mexico earthquake, *Geophys. J. Int.,* **169,** 389–406.

Selvans, M.M., Stock, J.M., DeMets, C., Sanchez, O. & Marquez-Azua, B., 2011. Constraints on Jalisco block motion and tectonics of the Guadalajara triple junction from 1998–2001 campaign GPS data, *Pure appl. Geophys.,* **168,** 1435–1447.

Shi, Q., Barbot, S., Wei, S., Tapponnier, P., Matsuzawa, T. & Shibazaki, B., 2020. Structural control and system-level behavior of the seismic cycle at the Nankai Trough, *Earth Planets Space,* **72**(1), 1–31.

Singh, S.K., Ponce, L. & Nishenko, S.P., 1985. The great Jalisco, Mexico, earthquakes of 1932: Subduction of the Rivera plate, *Bull. seism. Soc. Am.,* **75,** 1301–1314.

Suito, H. & Freymueller, J.T., 2009. A viscoelastic and afterslip postseismic deformation model for the 1964 Alaska earthquake, *J. geophys. Res.,* **114,** B11404, doi:1029/2008JB005954.

Trubienko, O., Fleitout, L., Garaud, J.-D. & Vigny, C., 2013. Interpretation of interseismic deformations and the seismic cycle associated with large subduction earthquakes, *Tectonophysics,* **589,** 126–141.

Wang, K., Hu, Y. & He, J., 2012. Deformation cycles of subduction earthquakes in a viscoelastic Earth, *Nature,* **484,** 327–332.

Watkins, W.D., Thurber, C.H., Abbott, E.R. & Brudzinski, M.R., 2018. Local earthquake tomography of the Jalisco, Mexico region, *Tectonophysics,* **724–725,** 51–64.

Wessel, P. & Smith, W.H.F., 1991. Free software helps map and display data, *EOS, Trans. Am. geophys. Un.,* **72**(41), 445–446.

SUPPORTING INFORMATION

Supplementary data are available at *GJI* online.

Locking_files.zip
Cosenza-Muralles_etal_2021-II_Supp_Information.pdf

Figure S1. Best-fitting GPS site velocities from the time-dependent inversion of GPS position time-series that were corrected for viscoelastic effects of the 1995 Colima–Jalisco and 2003 Tecoman earthquakes using $\tau_m = 2.5$ yr. (a) Horizontal velocities relative to a fixed NA plate frame of reference. Ellipses represent 2-D, 1σ uncertainties. (b) Vertical velocites. Thin black lines represent 1σ uncertainties. Colour shows the interpolated surface vertical velocities over the region.

Figure S2. Best-fitting GPS site velocities from the time-dependent inversion of GPS position time-series that were corrected for viscoelastic effects of the 1995 Colima–Jalisco and 2003 Tecoman earthquakes using $\tau_m = 4$ yr. (a) Horizontal velocities relative to a fixed NA plate frame of reference. Ellipses represent 2-D, 1σ uncertainties. (b) Vertical velocites. Thin black lines represent 1σ uncertainties. Colour shows the interpolated surface vertical velocities over the region.

Figure S3. Best-fitting GPS site velocities from the time-dependent inversion of GPS position time-series that were corrected for viscoelastic effects of the 1995 Colima–Jalisco and 2003 Tecoman earthquakes using $\tau_m = 8$ yr. (a) Horizontal velocities relative to a fixed NA plate frame of reference. Ellipses represent 2-D, 1σ uncertainties. (b) Vertical velocites. Thin black lines represent 1σ uncertainties. Colour shows the interpolated surface vertical velocities over the region.

Figure S4. Best-fitting GPS site velocities from the time-dependent inversion of GPS position time-series that were corrected for viscoelastic effects of the 1995 Colima–Jalisco and 2003 Tecoman earthquakes using $\tau_m = 15$ yr. (a) Horizontal velocities relative to a fixed NA plate frame of reference. Ellipses represent 2-D, 1σ uncertainties. (b) Vertical velocites. Thin black lines represent 1σ uncertainties. Colour shows the interpolated surface vertical velocities over the region.

Figure S5. Best-fitting GPS site velocities from the time-dependent inversion of GPS position time-series that were corrected for viscoelastic effects of the 1995 Colima–Jalisco and 2003 Tecoman earthquakes using $\tau_m = 25$ yr. (a) Horizontal velocities relative to a fixed NA plate frame of reference. Ellipses represent 2-D, 1σ uncertainties. (b) Vertical velocites. Thin black lines represent 1σ uncertainties. Colour shows the interpolated surface vertical velocities over the region.

Figure S6. Best-fitting GPS site velocities from the time-dependent inversion of GPS position time-series that were corrected for viscoelastic effects of the 1995 Colima–Jalisco and 2003 Tecoman earthquakes using $\tau_m = 40$ yr. (a) Horizontal velocities relative to a fixed NA plate frame of reference. Ellipses represent 2-D, 1σ uncertainties. (b) Vertical velocites. Thin black lines represent 1σ uncertainties. Colour shows the interpolated surface vertical velocities over the region.

Figure S7. Best-fitting GPS site velocities from the time-dependent inversion of GPS position time-series with no viscoelastic effects corrections. (a) Horizontal velocities relative to a fixed NA plate frame of reference. Ellipses represent 2-D, 1σ uncertainties. (b) Vertical velocites. Thin black lines represent 1σ uncertainties. Colour shows the interpolated surface vertical velocities over the region.

Figure S8. Panels (a) and (c) show a comparison between the best-fitting GPS site velocities from the time-dependent inversion of GPS position time-series that were corrected for viscoelastic effects of the 1995 Colima–Jalisco and 2003 Tecoman earthquakes using $\tau_m = 15$ yr (blue arrows), and the velocities estimated as the best-fitting 3D slopes for each station with measurements after 2010 from the original daily station positions, corrected only for the steady movement of the NA plate (red arrows). Ellipses in (a) represent 2-D, 1σ uncertainties of the horizontal velocities. Thin black lines in (c) represent 1σ uncertainties of the vertical velocities. Panels (b) and (d) show the difference of these velocities (horizontal and vertical, respectively) at each GPS site.

Please note: Oxford University Press is not responsible for the content or functionality of any supporting materials supplied by the authors. Any queries (other than missing material) should be directed to the corresponding author for the paper.